Mon. Not. R. Astron. Soc. **298,** 416–432 (1998)

A *ROSAT* study of the cores of clusters of galaxies – I. Cooling flows in an X-ray flux-limited sample

C. B. Peres, A. C. Fabian, A. C. Edge, S. W. Allen, R. M. Johnstone and D. A. White
Institute of Astronomy, Madingley Road, Cambridge CB3 0HA

Accepted 1998 March 11. Received 1998 January 20; in original form 1997 August 6

ABSTRACT

This is the first part of a study of the detailed X-ray properties of the cores of nearby clusters. We have used the flux-limited sample of 55 clusters listed by Edge et al., and archival and proprietary data from the *ROSAT* observatory. In this paper an X-ray spatial analysis based on the surface-brightness-deprojection technique is applied to the clusters in the sample with the aim of studying their cooling flow properties. We determine the fraction of cooling flows in this sample to be 70–90 per cent, and estimate the contribution of the flow region to the cluster X-ray luminosity. We show that the luminosity within a strong cooling flow can account for up to 70 per cent of a cluster X-ray bolometric luminosity. Our analysis indicates that about 40 per cent of the clusters in the sample have flows depositing more than 100 $M_{\odot}$ yr^{-1} throughout the cooling region, and that these possibly have been undisturbed for many Gyr, confirming that cooling flows are the natural state of cluster cores. New cooling flows in the sample are presented, and previously ambiguous ones are clarified. We have constructed a catalogue of some intracluster medium properties for the clusters in this sample. The profiles of the mass deposited from cooling flows are analysed, and evidence is presented for the existence of breaks in some of the profiles. Comparison is made to recent optical and radio data. We cross-correlate our sample with the Green Bank, NVSS and FIRST surveys, and with the volume-limited sample of brightest cluster galaxies presented by Lauer & Postman. Although weak trends exist, no strong correlation between optical magnitude or radio power of the brightest cluster galaxy and the strength of the flow is found.

Key words: galaxies: clusters: general – cooling flows – X-rays: galaxies.

1 INTRODUCTION

The X-rays emitted from clusters of galaxies represent a loss of energy of the intracluster gas. Thermal bremsstrahlung and line emission depend on the square of the gas density, which rises towards the cluster centre. As the density rises, the loss rate increases and the resultant cooling time-scale, $t_{\rm cool}$, decreases. Within the cooling radius ($r_{\rm cool}$), the cooling time becomes smaller than the age of the cluster ($t_{\rm cool} < t_{\rm age} \approx H_0^{-1}$) and, under gravity and thermal pressure, the gas cools and flows inward to maintain pressure equilibrium.

This simple picture describes the physics of a homogeneous cooling flow. In a more realistic situation, initial inhomogeneities in the intracluster medium (ICM) lead to the establishment of a multiphase atmosphere, which cools over a wide range of radii, depositing cool material through the central ~200 kpc of a cluster of galaxies. (For reviews on cooling flows, see Fabian, Nulsen & Canizares 1984 and Fabian 1994).

Although the mass cooling out of the X-ray band represents only a negligible amount when compared to the total hot phase of the ICM, it is comparable to the mass of a brightest cluster galaxy (BCG) for flows which are undisturbed for about a Hubble time. Understanding the physical processes of a cooling flow and of the fate of the cooled material is therefore of great importance for understanding the evolution of the core of a cluster.

Edge, Stewart & Fabian (1992) stress that the characterization of a cluster as a cooling flow depends heavily on the spatial resolution and sensitivity of the instruments used to image the cluster. This was the main limitation for early work.

ROSAT offers, so far, the best opportunity to resolve the cores of the clusters and thus establish in a reliable manner the fraction of cooling flows in a flux-limited sample. It also offers a unique opportunity to study the occurrence of substructure in cooling flows (Peres, Buote & Fabian, in preparation), and to resolve mass deposition and cooling time profiles. The low background contamination of one of its detectors, the Position Sensitive Proportional Counter (PSPC), allows surface brightness profiles to be extracted to a large radius. The good image capabilities of the other instrument, the High Resolution Imager (HRI), is important for the study of substructure and, in the context of the present work, fundamental for determining the properties of more distant flows.

Table 1. B55 sample. (a) Name of the cluster; (b) Right ascension of X-ray peak (J2000); (c) Declination of X-ray peak (J2000); (d) Right ascension of optical counterpart (J2000); (e) Declination of optical counterpart (J2000); (f) Offset between the X-ray and optical peaks, in arcsec; (g) Signal the present (√), absence (×), or lack of information (−) of optical emission lines; (h) Radio flux density (in mJy) at 6 cm from the Green Bank survey; (i) Radio flux density (in mJy) at 20 cm from the Green Bank (†), NVSS or FIRST (*) surveys. The values presented in columns (h) and (i) are for sources which are coincident with the optical or X-ray position within the angular resolution of the survey. We follow the convention used in (g) to indicate lack of information on radio fluxes.

Cluster	R.A. (X-ray)	Dec. (X-ray)	R.A. (opt.)	Dec. (opt.)	$\Delta\theta$	Opt. Lines	Flux (5 GHz)	Flux (1.4 GHz)
(a)	(b)	(c)	(d)	(e)	(f)	(g)	(h)	(i)
A85	00 41 50.8	−09 18 07	00 41 50.4	−09 18 12	8	√	(4.6±1.1)×10	(5.8±0.3)×10
A119	00 56 16.8	−01 14 45	00 56 16.1	−01 15 19	36	×	–	×
A262	01 52 45.4	36 09 26	01 52 46.5	36 09 06	24	√	–	$(1.31)\times10^2$ †
AWM7	02 54 27.4	41 34 51	02 54 27.5	41 34 46	5	×	–	–
A399	02 57 53.6	13 01 47	02 57 53.2	13 01 50	7	×	–	×
A401	02 58 56.0	13 35 03	02 58 57.8	13 34 57	27	×	–	×
A3112	03 17 57.7	−44 14 17	03 17 57.7	−44 14 18	1	×	$(6.9\pm0.4)\times10^2$	–
A426	03 19 48.0	41 30 46	03 19 48.3	41 30 41	6	√	$(4.2\pm0.5)\times10^4$	$(2.12)\times10^4$ †
2A 0335+096	03 38 40.2	09 58 12	03 38 40.6	09 58 11	6	√	–	(2.41±0.12)×10
A3158	03 42 50.9	−53 37 32	03 42 53.0	−53 37 53	28	×	–	–
A478	04 13 25.0	10 27 59	04 13 25.3	10 27 54	7	√	–	(3.55±0.15)×10
A3266	04 31 15.7	−61 27 08	04 31 13.5	−61 27 12	11	×	–	–
A496	04 33 37.6	−13 15 40	04 33 37.8	−13 15 43	4	√	(4.4±1.1)×10	–
3C129	———	———	04 48 58.2	45 02 01	–	–	–	$(5.31)\times10^3$
A3391	06 26 19.9	−53 41 53	06 26 20.4	−53 41 36	18	×	$(1.922\pm0.019)\times10^3$	–
A576	07 21 31.2	55 45 52	07 21 30.2	55 45 40	15	×	–	×
PKS 0745-191	07 47 30.9	−19 17 43	07 47 31.3	−19 17 40	6	√	$(4.8\pm0.3)\times10^2$	$(2.37\pm0.08)\times10^3$
A644	08 17 25.5	−07 30 40	08 17 25.6	−07 30 46	6	×	–	–
A754	09 09 18.8	−09 41 20	09 08 32.4	−09 37 49	691	×	–	$(9.0\pm1.0)\times10^0$
Hyd-A	09 18 05.8	−12 05 40	09 18 05.6	−12 05 44	5	√	$(1.40\pm0.01)\times10^4$	$(4.08\pm0.13)\times10^4$
A1060	10 36 43.2	−27 31 40	10 36 42.8	−27 31 41	6	√	–	×
A1367	11 44 48.2	19 42 05	11 44 48.0	19 41 18	47	×	–	×
Virgo	12 30 49.0	12 23 35	12 30 49.4	12 23 26	9	√	$(6.1\pm0.8)\times10^4$	$(2.24)\times10^4$ †
Cent	12 48 48.9	−41 18 44	12 48 49.1	−41 18 42	3	√	$(1.53\pm0.08)\times10^3$	–
Coma	12 59 35.6	27 57 31	12 59 35.6	27 57 34	6	×	(8.4±1.2)×10	$(2.07\pm0.07)\times10^2$
A1644	12 57 12.2	−17 24 34	12 57 11.6	−17 24 35	9	×	$(1.12\pm0.12)\times10^2$	(9.9±0.3)×10
A3532	12 57 21.8	−30 21 51	12 57 22.0	−30 21 50	3	–	$(4.4\pm0.3)\times10^2$	$(1.16\pm0.04)\times10^3$
A1650	12 58 41.7	−01 45 44	12 58 41.5	−01 45 41	4	–	–	–
A1651	12 59 21.7	−04 11 47	12 59 22.5	−04 11 46	12	×	–	–
A1689	13 11 29.5	−01 20 28	13 11 29.5	−01 20 29	1	×	–	×
A1736	13 26 50.0	−27 10 20	13 26 48.7	−27 08 37	103	×	–	×
A3558	13 27 56.5	−31 29 44	13 27 56.8	−31 29 45	4	×	–	$(4.5\pm0.5)\times10^0$
A3562	13 33 36.0	−31 40 05	13 33 34.7	−31 40 21	23	×	–	×
A3571	13 47 28.4	−32 51 55	13 47 28.3	−32 51 55	1	–	–	(8.4±1.7)
A1795	13 48 52.7	26 35 30	13 48 52.6	26 35 35	5	√	$(2.6\pm0.3)\times10^2$	$(9.3\pm0.3)\times10^2$ *
A2029	15 10 55.8	05 44 46	15 10 56.1	05 44 41	7	×	(8.9±1.4)×10	$(5.5)\times10^2$ †
A2052	15 16 43.7	07 01 19	15 16 44.6	07 01 17	13	√	$(1.03\pm0.14)\times10^3$	$(5.4)\times10^3$ †
MKW3s	15 21 51.8	07 42 24	15 21 51.9	07 42 30	6	√	–	$(1.26)\times10^2$ †
A2065	15 22 29.0	27 42 33	15 22 29.2	27 42 26	7	×	–	(1.4±0.3)×10
A2063	15 23 04.8	08 36 20	15 23 05.3	08 36 33	15	×	–	(1.5±0.07)×10
A2142	15 58 20.2	27 13 52	15 58 20.1	27 14 00	8	√	–	×
A2147	———	———	16 02 17.0	15 58 27	–	×	–	–
A2199	16 28 37.7	39 33 03	16 28 38.6	39 33 04	7	√	$(4.8\pm0.5)\times10^2$	$(3.7)\times10^3$ †
A2204	16 32 47.1	05 34 34	16 32 46.8	05 34 31	5	√	–	(7.01±0.2)×10
Tri Aust	16 38 20.3	−64 21 28	16 38 18.3	−64 21 36	20	–	–	–
A2244	17 02 41.9	34 03 30	17 02 42.5	34 03 35	9	×	–	$(2.41\pm0.13)\times10^0$ *
A2256	17 03 13.9	78 39 06	17 04 27.1	78 38 25	59	×	–	×
Ophiuchus	17 12 27.8	−23 22 08	17 12 28.2	−23 22 09	6	√	–	(2.91±0.1)×10
A2255	17 12 36.2	64 04 09	17 12 35.0	64 04 14	9	×	–	×
A2319	19 21 09.7	43 56 48	19 21 10.1	43 56 43	7	×	–	×
Cyg-A	19 59 28.1	40 44 05	19 59 28.4	40 44 01	5	√	$(2.1\pm0.3)\times10^5$	–
A3667	20 12 24.3	−56 49 49	20 12 27.4	−56 49 37	25	×	–	–
A2597	23 25 19.3	−12 07 20	23 25 19.7	−12 07 27	9	√	$(4.1\pm0.2)\times10^2$	$(1.88\pm0.06)\times10^3$
Klem44	23 47 43.4	−28 08 20	23 47 43.4	−28 08 37	17	–	–	(2.84±0.13)×10
A4059	23 57 00.2	−34 45 39	23 57 00.5	−34 45 35	5	√	$(1.17\pm0.13)\times10^2$	$(1.29\pm0.04)\times10^3$

In the absence of a volume-limited sample, statistical studies of cooling flows are best pursued with the use of a flux-limited sample, such as the one presented by Edge et al. (1990). The clusters in this sample are the brightest 55 over the sky in the 2–10 keV band (hereafter the B55 sample), and all have fluxes above 1.7×10^{-11} erg cm^{-2} s^{-1}. The clusters were selected from observations with the *Einstein* and *EXOSAT* observatories, and the *HEAO-1* and *Ariel V* satellites.

The work of Ebeling et al. (1996) on the X-ray Brightest Abell Cluster Sample (XBACS) showed that the completeness the B55 sample was satisfactory. A remaining issue in the analysis of cooling flow properties in this sample was the ability to image the

cooling region in the centres of clusters. Here we analyse *ROSAT* pointed observations of the clusters in the B55 sample and deproject their surface brightness profiles. This allows us to build a catalogue of the ICM and cooling flow properties of the B55 clusters, and to compare these to recent optical and radio data. The structure of the paper is as follows. In Sections 2 and 3 we describe the selection of the observations and the method of analysis, respectively. In Section 4 we present our results, and in Section 5 we summarize our conclusions. We assume throughout that $H_0 = 50$ km s^{-1} Mpc^{-1} and $q_0 = 0.5$.

2 OBSERVATIONS

We have used archival and proprietary observations of the B55 clusters carried out with the Position Sensitive Proportional Counter (PSPC) and the High Resolution Imager (HRI) on *ROSAT*. (The only exceptions were the cases of 3C 129 and A2147, for which no useful ROSAT observations exist.) The PSPC provides a FWHM spatial resolution of ~25 arcsec (corresponding to a scale of 60 kpc for objects at a redshift $z \sim 0.1$) and a FWHM spectral resolution of $\Delta E/E = 0.43(E/0.93\,\mathrm{keV})^{-0.5}$, whereas the HRI has a FWHM spatial resolution of ~4 arcsec and basically no spectral resolution.

The HRI is ideal for characterizing mass deposition profiles due to its high spatial resolution, wherreas the PSPC is invaluable for recovering ICM properties from the cluster surface brightness, due to its low and well-characterized background. In this work we have analysed 47 *ROSAT* PSPC observations, 38 *ROSAT* HRI observations (32 observations with both instruments), covering a total of 85 images of 53 clusters. When more than one observation existed for the same object with the same instrument, we used only the observation with the longest exposure time. (Only in a few cases were other criteria, e.g., the existence of a better centred image, considered more important.)

A list of the clusters in the B55 sample, together with relevant generic information, is displayed in Tables 1 and 2. The X-ray positions given in Table 1 correspond to the peak in X-ray emission from our data, and were found by visual inspection. The optical positions were determined from optical counterparts in images retrieved from the *Space Telescope* Digitized Sky Survey (DSS). (We have used the HRI images, whenever available, to determine the locus of the X-ray peak.) For cases where no clear single X-ray peak existed, like A1367 and A1736, the centroid of the X-ray emission was used. The close agreement between the optical and X-ray positions can be seen from their offset, $\Delta\theta$, presented in Table 1 (cf. Section 4.6).

The radio information in Table 1 was obtained by searching the Green Bank 1400- and 4850-MHz surveys (available through NED) and the 1400-MHz FIRST and NVSS on-line catalogues. The information on the existence of optical emission lines was obtained from a variety of sources in the literature and from private communication (C. S. Reynolds and C. S. Crawford).

The X-ray observations used are identified by their *ROSAT* Observation Request Sequence Number (ROR) in Table 2, where the raw exposure times and cluster redshifts for each observation are also listed. The other entries in this table are discussed in the next section.

3 METHOD OF ANALYSIS

We have undertaken the present analysis in two distinct stages: (i) the reduction of the data to produce one image per observation, and (ii) the deprojection of the azimuthally averaged surface brightness profiles extracted from these images.

In the first stage, PSPC images have been constructed from counts in the energy range 0.4–2.0 keV and have been vignetting-corrected. They have also been corrected for instrument and telemetry dead time, and had periods of high particle background and scattered solar X-rays removed. With the selection of this range of energies we minimize the Galactic and particle backgrounds (which dominate below 0.4 keV and above 2.1 keV respectively), while retaining most of the cluster emission. The vignetting and exposure-time corrections were performed using the IDL routines *make_emap.pro*, *make_image.pro*, *mexdiv.pro*; this follows the prescription of Snowden et al. (1994). The background subtraction of PSPC images was left to the deprojection software, written by D. White and collaborators. (We select the bin for which the background counts are accumulated by inspection of the azimuthally averaged surface brightness, which works very well for the PSPC due to its low background count rate.)

The HRI images were reduced in a different manner. Background subtraction was performed with the Starlink software ASTERIX, by accumulating counts in circles of approximately $0\overset{\circ}{.}05$ in a clear off-centre area of the image. The vignetting correction was left to the deprojection software. In all cases we were careful to inspect each background-subtracted surface brightness profile and only deproject it up to a point where the difference between the subtracted and non-subtracted values differ insignificantly. In this way we guarantee that background subtraction does not affect the results significantly.

For both the PSPC and HRI images we have identified contaminating sources by eye and masked them out (we have also masked out the detector supporting structure in the PSPC images). Finally, we have extracted the profile of counts in annuli around the peak of the X-ray emission to obtain a surface brightness profile suitable for deprojection. All the image analysis was carried out with ASTERIX and our deprojection software.

In the second stage we use the single-phase algorithm for surface brightness deprojection of Fabian et al. (1980), first used for the analysis of clusters of galaxies by Fabian et al. (1981).[1] In this technique counts in an X-ray image are assumed to come from a spherically symmetric (single-phase) hot thin plasma in hydrostatic equilibrium. Modelling the cluster emission as such allows us to obtain the emission from each spherical shell in the cluster from the observed surface brightness profile, and to compare this emission with the predicted value from a plasma code. (For this work we have used the MEKAL code; cf. Arnaud & Rothenflug 1985, Mewe, Gronenschild & van den Oord 1985, Mewe, Lemen & van den Oord 1986 and Kaastra 1992.) Through this comparison we can obtain the radial distribution of the thermodynamic properties of the gas in the ICM, namely temperature, pressure and electron density. Once these quantities are known, secondary properties like luminosity, central cooling time and mass deposition rates can be estimated. A more detailed exposition of the deprojection algorithm used here can be found in White, Jones & Forman (1997, and references therein).

The input parameters in the implementation of the deprojection algorithm used here are redshift of the cluster, average temperature (as measured by *Einstein* MPC, *EXOSAT* or *Ginga*; David et al. 1993), spectral band of the instrument (0.1–2.4 keV), Galactic

[1] A more sophisticated deprojection, taking into account the multiphase nature of the ICM, is known to give results in agreement with our simple approach here (Thomas, Fabian & Nulsen 1987).

Table 2. Input parameters for the deprojection analysis. (a) Name of the cluster. The letter inside brackets indicate whether the observation was made with the PSPC(P), or with the HRI(H); (b) *ROSAT* Observation Request Sequence Number (ROR); (c) Raw exposure time in seconds; (d) Redshift of the cluster; (e) Bin size (in kpc) used in the deprojection; (f) Galactic neutral hydrogen column density along the line of sight to the cluster, given in units of 10^{21} cm^{-2}; (g) Temperature (in keV) from the catalogues of David et al. (1993) and White et al. (1997); (h) Outer radius to which the surface brightness profile was extracted (in Mpc).

Cluster	ROR	Δt	z	bin size	$N_{\rm H}$	$\langle kT \rangle$	$R_{\rm out}$
(a)	(b)	(c)	(d)	(e)	(f)	(g)	(h)
A85(H)	rh800271	17308	0.0521	11.1	0.3	6.2	0.244
A85(P)	rp800250	10240	0.0521	41.5	0.3	6.2	0.914
A119(P)	rp800251	15203	0.044	35.6	0.35	5.1	1.049
A262(P)	rp800254	8719	0.0164	20.9	0.53	2.4	0.452
AWM7(H)	wh800364	14864	0.0172	3.8	0.92	3.6	0.140
AWM7(P)	wp800168	13335	0.0172	14.6	0.92	3.6	0.532
A399(H)	rh800850n00	6833	0.0715	73.5	1.17	5.8	0.757
A401(P)	rp800235	7465	0.0748	57.3	1.11	7.8	1.175
A3112(P)	rp800302n00	7600	0.0746	57.2	0.4	4.1	0.886
A3112(H)	rh800627a01	9540	0.0746	16.0	0.4	4.1	0.421
A426(H)	wh800068	10785	0.0183	5.93	1.45	5.5	0.090
A426(P)	wp800186	4787	0.0183	23.2	1.45	5.5	0.766
2A 0335+096(H)	rh800050	14012	0.0349	5.14	1.72	3.0	0.190
2A 0335+096(P)	wp800083	10346	0.0349	28.7	1.72	3.0	0.731
A3158(P)	rp800310	3022	0.0575	68.1	0.12	5.5	1.022
A478(H)	wh800091	22712	0.0882	17.6	1.36	6.8	0.520
A478(P)	wp800193	22139	0.0882	66.0	1.36	6.8	1.420
A3266(P)	wp800552n00	13560	0.0594	70.1	0.3	6.2	0.678
A3266(H)	rh800628n00	8202	0.0594	25.0	0.3	6.2	0.608
A496(H)	rh800272	14493	0.033	7.2	0.44	4.7	0.236
A496(P)	rp800024	8972	0.033	27.2	0.44	4.7	0.476
A3391(P)	wp800080	6781	0.0545	64.9	0.45	5.2	0.930
A576(H)	rh800727n00	10090	0.0381	16.6	0.56	4.3	0.236
PKS 0745-191(H)	wh800398n00	23385	0.1028	20.0	4.66	8.5	0.330
PKS 0745-191(P)	wp800623n00	10477	0.1028	75.1	4.66	8.5	1.464
A644(H)	rh800273n00	18668	0.0704	21.7	0.73	6.6	0.355
A644(P)	wp800379n00	10285	0.0704	81.5	0.73	6.6	0.897
A754(P)	rp800232n00	6359	0.0542	64.6	0.47	8.7	1.270
A754(H)	rh800768a01	37346	0.0542	23.0	0.47	8.7	0.466
HYD-A(H)	rh800132	27488	0.0522	5.21	0.48	3.8	0.100
HYD-A(P)	rp800318n00	18403	0.0522	62.4	0.48	3.8	0.894
A1060(P)	wp800200	15852	0.0124	21.2	0.5	3.3	0.365
A1060(H)	rh800632n00	14967	0.0124	11.0	0.5	3.3	0.160
A1367(P)	rp800153	18982	0.0215	45.2	0.22	3.5	0.533
VIRGO(H)	wh700214	14239	0.0037	1.2	0.25	2.4	0.050
VIRGO(P)	wp800187	10539	0.0037	4.8	0.25	2.4	0.159
CENT(H)	rh700320a01	16526	0.0109	4.8	0.8	3.6	0.090
CENT(P)	wp800192	7985	0.0109	14.0	0.8	3.6	0.331
COMA(P)	rp800005	22183	0.0232	29.2	0.09	8.0	0.865
COMA(H)	rh800242a04	37410	0.0232	16.0	0.09	8.0	0.250
A1644(H)	rh800851a01	10232	0.0474	15.2	0.47	4.7	0.137
A3532(P)	wp701155n00	8620	0.0585	69.2	0.62	4.4	0.876
A1650(H)	rh800852a01	6054	0.0845	25.5	0.15	5.5	0.297
A1651(P)	wp800353	7435	0.0846	63.7	0.17	7.0	1.243
A1689(P)	rp800248	13957	0.181	115.6	0.19	10.1	0.982
A1689(H)	rh800445n00	13094	0.181	33.0	0.19	10.1	0.823
A1736(H)	rh800853a01	13783	0.046	29.6	0.5	4.6	0.291
A3558(H)	wh800399	16792	0.0478	25.6	0.45	6.5	0.409
A3558(P)	wp800076	30213	0.0478	96.0	0.45	6.5	1.593
A3562(P)	rp800237n00	20202	0.0499	59.9	0.42	3.8	1.297
A3571(H)	rh800626n00	19460	0.0391	25.5	0.4	7.6	0.446
A3571(P)	rp800287	6072	0.0391	31.9	0.40	7.6	0.781
A1795(P)	rp800105n00	36273	0.0627	49.1	0.12	5.1	0.957
A1795(H)	rh800222a01	11097	0.0627	13.0	0.12	5.1	0.506

Table 2. – *continued*

Cluster	ROR	Δt	z	bin size	$N_{\rm H}$	$\langle kT \rangle$	$R_{\rm out}$
(a)	(b)	(c)	(d)	(e)	(f)	(g)	(h)
A2029(H)	rh150024	17757	0.0767	15.6	0.31	7.8	0.383
A2029(P)	rp800249	12550	0.0767	58.6	0.31	7.8	1.025
A2052(P)	rp800275	6215	0.0348	57.2	0.29	3.4	0.557
A2052(H)	rh800223n00	4429	0.0348	15.0	0.29	3.4	0.308
MKW3(P)	rp800128	9996	0.0449	72.5	0.29	3.0	0.562
MKW3(H)	rh800425n00	13502	0.0449	10.0	0.29	3.0	0.244
A2065(H)	rh800724n00	11780	0.0722	22.2	0.29	8.4	0.363
A2063(P)	wp800184	10198	0.0350	22.2	0.29	4.1	0.363
A2142(P)	wp150084	7740	0.0899	67.1	0.39	11	1.443
A2142(H)	rh800640n00	19785	0.0899	27	0.39	11	0.910
A2199(H)	wh800071	5222	0.030	19.9	0.09	4.7	0.195
A2199(P)	wp800644n00	41082	0.030	24.8	0.09	4.7	0.733
A2204(H)	rp800750n00	15488	0.1523	40.9	0.56	9.0	0.667
A2204(P)	rp800281	5359	0.1523	102.2	0.56	9.0	1.175
TRI AUST(P)	rp800280n00	7338	0.051	40.7	1.98	7.9	0.916
A2244(P)	rp800265n00	2965	0.1024	112.2	0.2	7.1	0.935
A2256(P)	wp100110	17865	0.0581	45.8	0.43	7.5	1.169
A2256(H)	rh800676n00	43567	0.0581	25.0	0.43	7.5	0.745
OPHI(P)	rp800279n00	3932	0.028	23.3	1.97	9.0	0.756
OPHI(H)	wh800067	22285	0.028	9.3	1.97	9.0	0.202
A2255(P)	rp800512n00	14555	0.0809	92.0	0.26	7.3	1.258
A2319(H)	wh800072	5559	0.0564	29.7	0.86	9.9	0.303
A2319(P)	wp800073a01	3171	0.0564	44.6	0.86	9.9	1.138
CYG-A(H)	rh800021	43240	0.057	24.0	3.61	7.3	0.390
CYG-A(P)	wp800622n00	9447	0.057	67.6	3.61	7.3	1.464
A3667(P)	rp800234n00	12560	0.0530	42.2	0.4	6.5	1.328
A2597(H)	rh800111	17996	0.0824	24.9	0.25	6.0	0.241
A2597(P)	rp800112	7243	0.0824	62.3	0.25	6.0	0.904
KLEM44(P)	wp800354n00	3353	0.0283	23.5	0.15	3.3	0.505
A4059(H)	rh800224n00	6320	0.0478	15.3	0.11	3.5	0.190
A4059(P)	wp800175	5514	0.0478	38.4	0.11	3.5	0.595

hydrogen column density along the cluster line of sight, bin size of the data, H_0 and q_0, pressure at the outermost bin, cluster core radius and velocity dispersion, galaxy linear mass (GLM), and galaxy linear mass cut-off (GCTOF).[2] From these, only four are kept free to fit the X-ray data: the cluster core radius and velocity dispersion, GLM and GCTOF.[3] We model the potential as an isothermal sphere, adjusting the cluster core radius and velocity dispersion to conform to this model. This follows the works of Fukazawa et al. (1994) and Allen, Fabian & Kneib (1996). The former showed that the hot ICM phase exists up to the central parts of clusters of galaxies, while the latter showed that a consistent modeling of the cluster potential is achieved by assuming a roughly constant average temperature. This is discussed at length in Section 3.1.

Galactic absorption was accounted for by using the hydrogen column densities quoted by Stark et al. (1992). No excess column density was introduced in our analysis, although this was found to exist from the X-ray spectroscopic studies of cooling flow clusters (White et al. 1991; Allen & Fabian 1997). Any excess absorption increases the mass deposition rates, since the luminosity must be increased to produce the observed counts.

We have usually rebinned the PSPC and HRI data to 30 and 8 arcsec, respectively, to minimize complexities associated with the instrument PSF (there are cases with coarser binning. The exact bin size used for each case can be found in Table 2). Most of the values used for the average temperature were taken from David et al. (1993), although more recent data were used when available. The value used for A2597 is 6.0 keV.

We have used a Monte Carlo algorithm to perturb and deproject each surface brightness profile 100 times. By doing so, we can place limits on the quantities derived from the deprojection analysis. However, we stress that these limits should be associated with the assumed potential only. Systematic errors in the potential will lead to larger uncertainties in the derived quantities.

As a final remark, we note that the ICM is assumed to be in hydrostatic equilibrium. This is a key assumption needed to integrate the cooling flow equations, once a gravitational potential is assumed. It is reasonable, since the sound crossing time is usually shorter than the age of the cluster, which we assume to be $\sim H_0^{-1}$. Supportive evidence for this and for the hypothesis that the temperature profile is roughly constant is given below.

3.1 The multiphase (inhomogeneous) intracluster medium

Suggestive evidence that the highest temperature does not vary much with radius appeared in the work of Fukazawa et al. (1994), where the Centaurus cluster was observed with the *ASCA* satellite. They showed that hot components of the ICM exist through the

[2] The gravitational model for the galaxy has a linearly increasing mass profile and a cut-off radius to avoid runaway. This is analogous to the model assumed by Thomas et al. (1987).

[3] Three caveats must be mentioned here. (1) Although we keep the value of the velocity dispersion free, the values used are roughly in agreement with (at least the lower limits of) the values measured by optical studies (cf. Zabludoff, Huchra & Geller 1990 and Fadda et al. 1996). (2) The pressure at the outermost bin is not considered as a free parameter, since it is always adjusted for the temperature at the outermost bin to agree roughly with the averaged value. (3) The parameters of the central cluster galaxy do not sensitively affect the results presented here in most cases, due to the resolution of the data.

central 5 arcmin (∼130 kpc) of this cluster. By fitting a two-temperature Raymond–Smith (RS) model to the data, these authors showed that the temperature profile for the cluster is approximately constant up to the inner ∼2 arcmin (∼50 kpc). A study of the cluster of galaxies A1060 by Tamura et al. (1996) reached similar conclusions.

The hypothesis that the cluster temperature profile can be modelled as approximately flat received definitive support from the work of Allen et al. (1996), who studied the cluster PKS 0745 − 191 (hereafter 0745) with X-ray (spectral and imaging) and gravitational lensing methods. By carrying out a spatial analysis similar to ours, they showed that the deprojected gravitational mass is in agreement with the mass inferred from the modelling of the lens, provided that the temperature profile is assumed to be flat. In the study by Allen et al. additional supporting evidence for the assumption of a flat temperature profile was obtained by spectroscopy. The X-ray spectrum of 0745, taken with *ASCA*, was only reasonably fitted if a two-temperature or a CFLOW model[4] were used. From this analysis Allen et al. showed that once the effects of the cooling flow are taken into account in the spectral analysis (through the CFLOW model) the cluster is observed to be approximately isothermal. Comparing the X-ray and lensing results for 0745, they conclude that the temperature profile should remain approximately isothermal up to ∼10 arcsec (instead of the 2-arcmin limit obtained from the *ASCA* data alone).

From the work of Allen et al. (1996) it is clear that the assumption of an isothermal profile for the gas makes the single-phase deprojection analysis appropriate for modelling the true multiphase nature of the ICM and the cluster gravitational potential[5] (gravitational lensing was used as a cross-check). For the clusters in this sample we cannot resort to the approaches discussed above to cross-check the appropriateness of our models, since spatially resolved spectroscopic information is not available for most of the B55 clusters, and their redshifts and masses are not suitable for gravitational lensing studies. However, two indications of the appropriateness of our method are (i) the size of the mass core radii we obtain for the B55 clusters, and (ii) the functional form of the mass deposition rate profile inferred from the analysis.

The values of mass core radii for the B55 clusters used in our analyses are available from Table 3 and are plotted in Fig. 1. They were obtained from our requirement that the mean X-ray gas temperature stay approximately constant, as the evidence presented above suggests. This methodology produces core radii which are overall smaller than ones found in previous analyses (Edge et al. 1992; White et al. 1997) where different assumptions were used. Our findings agree with the trend of smaller core radii found from gravitational lensing studies of more distant clusters, and with the multiphase picture of the ICM (Fabian et al. 1984; see also recent work of Waxman & Miralda-Escudé 1995).

Our model of the cluster gravitational potential includes a separate mass component for the central galaxy. Despite this extra complication, it is interesting to note from Fig. 1 that there is a clear separation between cooling-flow and non-cooling-flow clusters. This is supported by the X-ray/lensing analysis of Allen (1998).

The widespread deposition of material over the cluster core also corroborates the multiphase nature of the ICM, where various different phases drop out of the flow at different radii. In fact, simple multiphase models proposed by Nulsen (1986) find $\dot{M}(< r) \sim r^{\alpha}$, with $\alpha \sim 1$ (cf. Section 4.4).

Table 3. Parameters for modelling the cluster potential. (a) cluster name, (b) cluster velocity dispersion (in km s^{-1}), (c) cluster core radius (in kpc), (d) linear galaxy mass (in 10^8 $M_{\odot}$ pc^{-3}), (e) cut-off for the galaxy mass (in Mpc). Note that the profile for the Coma cluster was fitted with a single isothermal model.

Cluster	$\sigma_{\rm deproj}$	$a_{\rm deproj}$	GLM	GCTOF
A85	700	130	2.0	0.06
A119	680	600	1.0	0.08
A262	450	130	1.2	0.04
AWM7	520	200	1.1	0.08
A399	940	550	1.0	0.10
A401	950	350	0.8	0.08
A3112	670	120	1.4	0.06
A426	700	60	0.9	0.06
2A 0335+096	600	40	0.1	0.05
A3158	860	400	0.8	0.08
A478	850	180	1.8	0.08
A3266	780	500	1.5	0.17
A496	610	60	1.2	0.05
A3391	750	300	0.8	0.08
A576	700	150	0.6	0.06
PKS 0745-191	1050	100	1.5	0.08
A644	860	200	0.6	0.08
A754	800	300	1.6	0.09
HYD-A	680	220	1.8	0.07
A1060	500	150	0.7	0.09
A1367	700	500	0.4	0.03
VIRGO	600	90	1.0	0.02
CENT	400	120	1.6	0.06
COMA	1000	500	–	–
A1644	700	180	1.8	0.08
A3532	660	350	0.8	0.12
A1650	600	100	0.8	0.08
A1651	900	220	1.0	0.12
A1689	1150	200	1.4	0.15
A1736	800	700	1.2	0.05
A3558	970	600	2.0	0.15
A3562	550	180	0.8	0.12
A3571	850	220	1.1	0.08
A1795	710	70	0.5	0.07
A2029	920	100	0.8	0.06
A2052	550	200	2.1	0.08
MKW3s	550	100	0.8	0.08
A2065	750	200	2.1	0.10
A2063	600	150	1.0	0.08
A2142	1050	200	1.8	0.12
A2199	670	150	1.3	0.08
A2204	1100	80	1.0	0.08
TRI AUST	800	220	2.5	0.05
A2244	930	150	0.5	0.05
A2256	920	550	0.9	0.15
OPHI	880	220	2.5	0.06
A2255	1000	650	0.5	0.07
A2319	870	180	0.4	0.08
CYG-A	850	50	2.5	0.05
A3667	730	250	0.5	0.04
A2597	850	100	1.6	0.10
KLEM44	550	100	0.6	0.08
A4059	560	110	0.4	0.09

[4] This is the same model used in this paper and described in Section 3. It is assumed that at each radial bin there is (i) gas in a single phase in hydrostatic equilibrium, and (ii) gas cooling out of the flow.

[5] Allen et al. (1996) did not use a full multiphase deprojection method, resorting only to an additional cooling flow component (CFLOW) in their spectral analysis. This is exactly the component present in our single-phase deprojection algorithm, and it simulates a whole range of phases cooling out of the X-ray band. Thomas et al. (1987) were able to show, through a study of 11 clusters, that the single-phase deprojection method gives results in accordance with a multiphase treatment, where more than one phase (apart from the material which is dropping out of the flow) exists at each radial bin.

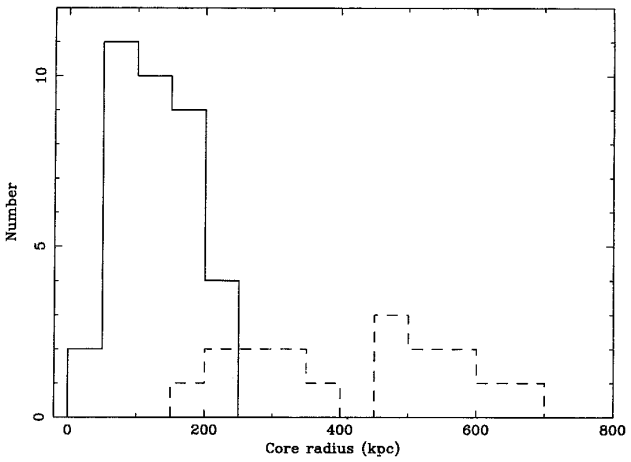

Figure 1. The distribution of core radii in the B55 sample shows the same bimodality found by the X-ray and lensing studies of Allen (1998). Cooling flows (solid line) have smaller core radii overall and show a distribution peaked around 100 kpc. Non-cooling-flows (dashed line) display a broader distribution of values, usually above 300 kpc.

Table 4. New cooling flows in the B55 sample. The values quoted for $\dot{M}$, $r_{\rm cool}$, and $t_{\rm cool}$ are median, 10 and 90 percentile estimates from the deprojection algorithm. The units used for $\dot{M}$, $r_{\rm cool}$ and $t_{\rm cool}$ are $M_\odot$ yr^{-1}, kpc and Gyr respectively.

Cluster	z	$\dot{M}$	$r_{\rm cool}$	$t_{\rm cool}$
Klem 44	0.0283	87^{+25}_{-19}	133^{+42}_{-27}	$2.3^{+0.6}_{-0.3}$
A1650	0.0845	280^{+464}_{-89}	165^{+103}_{-24}	$2.4^{+1.2}_{-0.8}$
A1651	0.0846	138^{+48}_{-41}	127^{+32}_{-31}	$6.5^{+0.7}_{-0.7}$
A2204	0.1523	852^{+127}_{-82}	199^{+60}_{-44}	$3.1^{+0.1}_{-0.1}$
A2065	0.0722	13^{+14}_{-6}	56^{+22}_{-23}	$4.4^{+2.2}_{-1.3}$
A3558	0.0478	40^{+39}_{-10}	68^{+75}_{-20}	$10.2^{+0.3}_{-0.2}$

4 RESULTS/DISCUSSION

The deprojected profiles of all clusters analysed by us cannot be presented here due to space limitations. Instead, we present a list with the input parameters necessary to reproduce the analyses in Tables 3 and 1. The results are displayed in a catalogue form in Table 5 and discussed in the next subsections.

4.1 X-ray luminosity

In Fig. 2 we plot the bolometric X-ray luminosity against total mass deposition rate. The bolometric luminosity was retrieved from the work of David et al. (1993) and the mass deposition rates come from our analysis. We have used HRI observations here only when no PSPC observation was available. From this plot we notice that the upper left and the lower right corners are not populated. The former can be taken as an expression of the fact that for a given X-ray luminosity there is always a maximal mass deposition rate. (Note that the cooling luminosity $L_{\rm cool} \sim \dot{M} \times T$.) The latter gives us a clear indication that very luminous systems harbour massive flows.

We have also investigated how much of the total bolometric luminosity can be attributed to the flow for each cluster in the sample. To answer this question, we computed the luminosity from

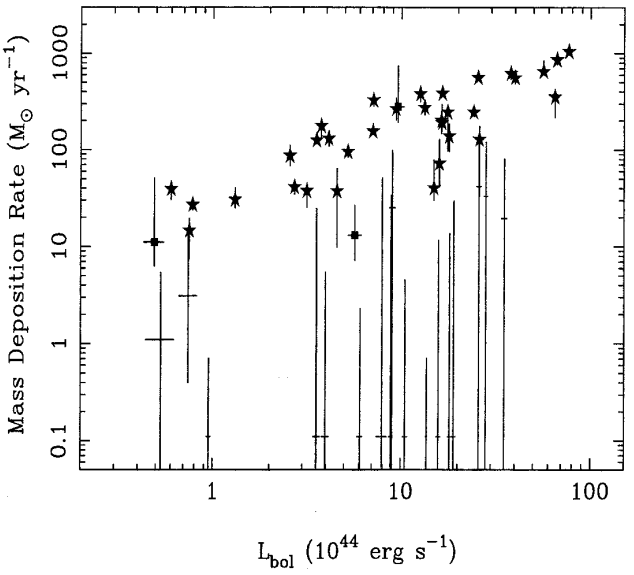

Figure 2. Mass deposition rate versus bolometric X-ray luminosity for the clusters in our sample. The lack of points in the upper left corner only reflects the maximum $\dot{M}$ allowed for a given luminosity. Stars are used to denote PSPC observations. Squares represent the clusters for which only HRI observations were available. No special symbols are used to denote the clusters which have mass deposition rates consistent with zero. The error bars for these clusters extend to the bottom of the figure and are kept to indicate the upper limit in their mass deposition rates. (When the median mass deposition is zero, we assume it equal to 0.1 for display purposes.) The luminosity of the Virgo cluster was taken from White et al. (1998).

within the cooling radius, $L(< r_{\rm cool})$,[6] and plotted it against the bolometric X-ray luminosity given by David et al. (1993) in Fig. 3. We find that, despite the spread, 20 per cent of the clusters have 50 per cent or more of their bolometric X-ray luminosity produced in a region $< r_{\rm cool}$. The cooling flow region in A2204 contributes more than 70 per cent to the cluster's total X-ray luminosity. The percentages for the other clusters are listed in Table 5.

The approach described in the last paragraph does not treat non-cooling-flows properly, since the concept of a cooling radius, $r_{\rm cool}$, in this case is meaningless. To compare cooling flows and non-cooling-flow clusters, we have computed the fraction of the total luminosity coming from a central region of 100-kpc radius. This quantity, f_{100}, is plotted against $\dot{M}$ in Fig. 4, from which it is clear that (i) non-cooling-flows have an overall smaller fraction of their X-ray luminosity emitted from the centre ($f_{100} \sim 1$–10 per cent), when compared to cooling-flows ($f_{100} \sim 5$–50 per cent; clusters with massive cooling flows show $f_{100} > 15$ per cent), and (ii) a trend of increasing f_{100} with $\dot{M}$ is indicated by the plot. Some of these issues were investigated previously by Edge (1987) and White et al. (1997) but, to our knowledge, this is the first systematic investigation on the fraction of a cluster luminosity contributed by its core, undertaken with *ROSAT*.

We note that the large contribution to the X-ray bolometric luminosity emerging from within the inner ~200 kpc of a cooling flow cluster must have an influence on its detectability in imaging surveys (Pesce et al. 1990) and on the scatter in the $L_{\rm x}$–$T_{\rm x}$ correlation (Fabian et al. 1994).

[6] Note that $L(< r_{\rm cool})$ includes direct cooling and the gravitational work done on the gas; direct cooling accounts for only about half of $L(< r_{\rm cool})$.

Table 5. Summary of some deprojection results. (a) Name of the cluster. The letter inside brackets indicates whether the observation was made with the PSPC(P), or with the HRI(H); (b) Integrated mass deposition rate in units of $M_\odot$ yr^{-1}; (c) Cooling radius in units of kpc; (d) Central cooling time in units of Gyr; (e) X-ray bolometric luminosity within the cooling radius, $L(< r_{\rm cool})$, in units of 10^{44} erg s^{-1}; (f) Ratio of $L(< r_{\rm cool})$ to $L_{\rm bol}$. The values of $L_{\rm bol}$ are from David et al. (1993); (g) Cooling time of the bin encompassing the 250-kpc radius in units of Gyr; (h) Gas mass out to 0.5 Mpc or 0.25 (†) Mpc, in units of 10^{12} $M_\odot$; (i) Gravitational mass out to 0.5 Mpc or 0.25 (†) Mpc, in units of 10^{12} $M_\odot$; (j) Approximate ratio (percentage) of gas-to-gravitational mass inside 0.5 or 0.25 (†) Mpc.

Cluster	$\dot{M}$	$r_{\rm cool}$	$t_{\rm cool}$	$L(< r_{\rm cool})$	$\frac{L(<r_{\rm cool})}{L_{\rm bol}}$	t_{250}	$M_{\rm gas}$	$M_{\rm grav}$	$\frac{M_{\rm gas}}{M_{\rm grav}}$
(a)	(b)	(c)	(d)	(e)	(f)	(g)	(h)	(i)	(j)
A85(H)	107^{+294}_{-31}	93^{+111}_{-10}	$1.0^{+0.2}_{-0.1}$	$2.7^{+3.7}_{-0.2}$	$0.17^{+0.23}_{-0.01}$	– – – –	– – – –	– – – –	– – – –
A85(P)	198^{+53}_{-52}	146^{+41}_{-41}	$2.4^{+0.1}_{-0.1}$	$4.8^{+1.1}_{-1.2}$	$0.30^{+0.07}_{-0.07}$	$30.8^{+2.3}_{-2.7}$	31.2±0.5	166	19±0.3
A119(P)	0^{+2}_{-0}	0^{+62}_{-0}	$19.2^{+12.2}_{-8.6}$	0^{+0}_{-0}	0	$64.5^{+2.0}_{-1.2}$	15.5±0.5	89	18±0.6
A262(P)	27^{+4}_{-3}	104^{+11}_{-10}	$1.5^{+0.1}_{-0.1}$	$0.3^{+0.02}_{-0.02}$	$0.35^{+0.02}_{-0.02}$	$34.9^{+9.9}_{-5.4}$	2.5±0.0†	33†	8†
AWM7(H)	18^{+123}_{-11}	78^{+91}_{-21}	$0.6^{+0.2}_{-0.1}$	$0.3^{>0.7}_{-0.1}$	$0.11^{+0.25}_{-0.04}$	– – – –	– – – –	– – – –	– – – –
AWM7(P)	41^{+6}_{-6}	103^{+5}_{-8}	$1.9^{+0.2}_{-0.2}$	$0.5^{+0.03}_{-0.04}$	$0.18^{+0.01}_{-0.01}$	$28.0^{+6.6}_{-3.2}$	15.4±0.2	89	17±0.2
A399(H)	0.0^{+51}_{-0}	0^{+110}_{-0}	$15.2^{+8.4}_{-5.0}$	$0^{+0.7}_{-0}$	$0^{+0.04}_{-0}$	$35.1^{+10.1}_{-7.2}$	22.2±1.5	163	14±0.9
A401(P)	42^{+82}_{-42}	77^{+66}_{-77}	$10.6^{+4.0}_{-1.8}$	$0.9^{+1.6}_{-0.9}$	$0.03^{+0.05}_{-0.03}$	$22.5^{+2.1}_{-1.7}$	35.3±0.7	235	15±0.3
A3112(P)	376^{+80}_{-61}	192^{+65}_{-48}	$1.9^{+0.1}_{-0.1}$	$7.0^{+1.2}_{-1.2}$	$0.61^{+0.10}_{-0.10}$	$20.4^{+2.2}_{-1.8}$	26.7±0.6	140	19±0.4
A3112(H)	415^{+252}_{-174}	183^{+38}_{-8}	$0.7^{+0.1}_{-0.1}$	$7.8^{+0.3}_{-0.7}$	$0.68^{+0.02}_{-0.06}$	$12.5^{+6.9}_{-2.0}$	10.1±0.3†	75†	13±0.4†
A426(H)	>427	>78	$0.6^{+0.1}_{-0.1}$	>6.8	>0.29	– – – –	– – – –	– – – –	– – – –
A426(P)	556^{+33}_{-24}	185^{+11}_{-11}	$0.9^{+0.0}_{-0.0}$	$13.7^{+0.4}_{-0.4}$	$0.59^{+0.02}_{-0.02}$	$20.5^{+1.8}_{-1.7}$	34.4±0.4	130	26±0.3
2A 0335+096(H)	242^{+234}_{-32}	132^{+93}_{-21}	$0.6^{+0.4}_{-0.2}$	$3.8^{+1.3}_{-0.3}$	$0.55^{+0.19}_{-0.04}$	– – – –	– – – –	– – – –	– – – –
2A 0335+096(P)	325^{+32}_{-43}	215^{+29}_{-29}	$0.9^{+0.0}_{-0.0}$	$5.0^{+0.3}_{-0.3}$	$0.73^{+0.04}_{-0.04}$	$19.2^{+2.9}_{-3.2}$	18.5±0.5	86	22±0.6
A3158(P)	25^{+74}_{-25}	65^{+105}_{-65}	$12.0^{+4.2}_{-2.5}$	$0.4^{+1.0}_{-0.4}$	$0.05^{+0.12}_{-0.05}$	$24.6^{+2.8}_{-2.1}$	26.9±0.7	194	14±0.4
A478(H)	520^{+111}_{-107}	192^{+10}_{-5}	$1.1^{+0.2}_{-0.1}$	$14.5^{+0.5}_{-0.3}$	$0.32^{+0.01}_{-0.01}$	$16.3^{+3.8}_{-3.4}$	13.9±0.4†	108†	13±0.4†
A478(P)	616^{+63}_{-76}	204^{+27}_{-38}	$2.8^{+0.1}_{-0.1}$	$17.3^{+1.7}_{-2.7}$	$0.38^{+0.04}_{-0.06}$	$15.3^{+0.5}_{-0.5}$	44.1±0.5	272	16±0.2
A3266(P)	0^{+34}_{-0}	0^{+105}_{-0}	$13.7^{+1.8}_{-1.1}$	$0^{+0.7}_{-0}$	$0^{+0.04}_{-0}$	$42.7^{+3.9}_{-3.9}$	29.4±0.5	163	18±0.3
A3266(H)	$3.8^{+35}_{-3.8}$	35^{+78}_{-35}	$5.2^{+8.4}_{-1.5}$	$0.1^{+0.03}_{-0.03}$	0.5^{+0}_{-0}	$43.3^{+45.2}_{-5.2}$	22.1±1.6	146	15±1.1
A496(H)	95^{+37}_{-34}	103^{+16}_{-5}	$0.8^{+0.2}_{-0.1}$	$1.9^{+0.2}_{-0.1}$	$0.32^{+0.03}_{-0.02}$	– – – –	– – – –	– – – –	– – – –
A496(P)	95^{+13}_{-12}	110^{+12}_{-15}	$1.8^{+0.1}_{-0.1}$	$2.0^{+0.1}_{-0.2}$	$0.33^{+0.02}_{-0.03}$	$38.4^{+6.7}_{-6.1}$	6.5±0.1†	63†	10±0.2†
A3391(P)	0^{+5}_{-0}	0^{+32}_{-0}	$16.7^{+5.6}_{-3.5}$	$0.0^{+0.1}_{-0}$	$0^{+0.02}_{-0}$	$37.0^{+5.5}_{-3.1}$	16.1±0.5	161	10±0.3
A576(H)	3^{+13}_{-3}	37^{+38}_{-29}	$2.8^{+2.4}_{-0.9}$	$0.1^{+0.1}_{-0.0}$	$0.03^{+0.03}_{-0}$	– – – –	– – – –	– – – –	– – – –
PKS 0745-191(H)	787^{+368}_{-73}	188^{+23}_{-16}	$0.9^{+0.2}_{-0.1}$	$34.9^{+1.8}_{-1.8}$	$0.58^{+0.03}_{-0.03}$	$21.7^{+19.8}_{-6.4}$	18.0±0.7†	149†	12±0.5†
PKS 0745-191(P)	1038^{+116}_{-68}	214^{+49}_{-25}	$2.2^{+0.1}_{-0.1}$	$43.6^{+4.6}_{-2.8}$	$0.73^{+0.08}_{-0.05}$	$18.3^{+1.1}_{-1.2}$	55.7±1.1	329	17±0.3
A644(H)	216^{+48}_{-59}	167^{+18}_{-24}	$4.5^{+4.2}_{-1.7}$	$4.5^{+0.6}_{-1.0}$	$0.23^{+0.03}_{-0.05}$	$25.6^{+19.3}_{-6.2}$	9.3±0.4†	92†	10±0.4†
A644(P)	189^{+106}_{-35}	141^{+62}_{-18}	$6.8^{+0.4}_{-0.4}$	$4.1^{+2.3}_{-0.6}$	$0.21^{+0.12}_{-0.03}$	$26.1^{+1.4}_{-1.0}$	37.2±0.5	253	15±0.2

4.2 New cooling flows in the sample

We present in Table 5 the mass deposition rate, cooling radius and central cooling time for the clusters which did not feature this information in the Edge et al. (1992) paper. Three interesting cases are A2065, A1650 and A2204. In the first two cases, the resolution of the data in the Edge et al. paper hid a modest and a large cooling flow. The third case (A2204) is a massive cooling flow. A summary of the deprojection results for this cluster is presented in Fig. 5. (A2204 was observed with the *ROSAT* PSPC from 1992 September

Table 5 – *continued*

Cluster	$\dot{M}$	$r_{\rm cool}$	$t_{\rm cool}$	$L(<r_{\rm cool})$	$\frac{L(<r_{\rm cool})}{L_{\rm bol}}$	t_{250}	$M_{\rm gas}$	$M_{\rm grav}$	$\frac{M_{\rm gas}}{M_{\rm grav}}$
(a)	(b)	(c)	(d)	(e)	(f)	(g)	(h)	(i)	(j)
A754(P)	0^{+29}_{-0}	0^{+97}_{-0}	$15.0^{+3.1}_{-2.2}$	$0^{+0.7}_{-0}$	$0^{+0.04}_{-0}$	$46.7^{+6.8}_{-3.9}$	24.3±0.5	189	13±0.3
A754(H)	2^{+5}_{-2}	26^{+31}_{-26}	$7.9^{+9.7}_{-2.1}$	0^{+0}_{-0}	0^{+0}_{-0}	$36.6^{+7.4}_{-5.4}$	5.9±0.2	48	12±0.4
HYD-A(H)	>298	>167	$1.1^{+0.1}_{-0.1}$	>4.7	>0.51	– – –	– – –	– – –	– – –
HYD-A(P)	264^{+81}_{-60}	162^{+56}_{-68}	$2.0^{+0.0}_{-0.0}$	$4.7^{+1.0}_{-1.2}$	$0.52^{+0.11}_{-0.13}$	$21.0^{+1.1}_{-1.0}$	26.5±0.3	166	16±0.2
A1060(P)	15^{+5}_{-7}	79^{+15}_{-26}	$4.7^{+0.4}_{-0.3}$	$0.15^{+0.04}_{-0.1}$	$0.23^{+0.06}_{0.15}$	$39.9^{+3.7}_{-2.9}$	2.8±0.0†	40†	7†
A1060(H)	8^{+3}_{-2}	64^{+9}_{-13}	$3.2^{+1.2}_{-0.8}$	$0.1^{+0.01}_{-0.01}$	$15^{+1.5}_{-1.5}$	– – –	– – –	– – –	
A1367(P)	0^{+1}_{-0}	0^{+23}_{-0}	$25.8^{+13.1}_{-8.0}$	0	0	$44.1^{+3.9}_{-3.4}$	2.5±0.0†	23†	11†
VIRGO(H)	>12	>28	$0.1^{+0.0}_{-0.0}$	>0.1	>0.37	– – –	– – –	– – –	– – –
VIRGO(P)	39^{+2}_{-9}	102^{+6}_{-4}	$0.2^{+0.0}_{-0.0}$	$0.3^{+0.01}_{-0.01}$	∼0.5	– – –	– – –	– – –	– – –
CENT(H)	>24	>67	$0.4^{+0.0}_{-0.0}$	>0.4	$0.41_{>0.1}$	– – –	– – –	– – –	– – –
CENT(P)	30^{+10}_{-5}	81^{+23}_{-18}	$0.8^{+0.0}_{-0.0}$	$0.5^{+0.1}_{-0.1}$	$0.41^{+0.1}_{-0.1}$	$43.2^{+14.3}_{-8.1}$	3.2±0.1†	34†	9±0.3†
COMA(P)	0^{+1}_{-0}	0^{+15}_{-0}	$17.7^{+6.7}_{-4.1}$	0^{+0}_{-0}	0	$35.5^{+2.0}_{-1.8}$	27.8±0.2	220	13±0.1
COMA(H)	0^{+2}_{-0}	20^{+19}_{-20}	$7.3^{+5.2}_{-1.9}$	0.01^{+0}_{-0}	0	– – –	– – –	– – –	– – –
A1644(H)	11^{+40}_{-5}	58^{+56}_{-20}	$2.2^{+0.7}_{-0.6}$	$0.2^{+0.2}_{-0.1}$	$0.04^{+0.04}_{-0.02}$	– – –	– – –	– – –	– – –
A3532(P)	0^{+25}_{-0}	0^{+104}_{-0}	$14.0^{+3.3}_{-2.3}$	$0^{+0.3}_{-0}$	$0^{+0.08}_{-0}$	$40.8^{+8.2}_{-5.9}$	18.2±0.6	132	14±0.5
A1650(H)	280^{+464}_{-89}	165^{+103}_{-24}	$2.4^{+1.2}_{-0.8}$	$5.4^{+4.1}_{-0.9}$	$0.34^{+0.26}_{-0.06}$	$13.0^{+3.7}_{-3.3}$	10.1±0.6†	60†	17±1†
A1651(P)	138^{+48}_{-41}	127^{+32}_{-31}	$6.5^{+0.7}_{-0.7}$	$3.3^{+1.0}_{-1.0}$	$0.14^{+0.04}_{-0.04}$	$25.4^{+2.2}_{-2.0}$	29.9±0.6	250	12±0.2
A1689(P)	645^{+196}_{-42}	191^{+103}_{-13}	$5.7^{+0.2}_{-0.2}$	$26.1^{+9.5}_{-1.5}$	$0.43^{+0.16}_{-0.02}$	$22.8^{+1.2}_{-0.9}$	64.6±0.9	476	14±0.2
A1689(H)	484^{+275}_{-93}	162^{+73}_{-21}	$2.5^{+0.8}_{-0.5}$	$18.0^{+1.0}_{-1.0}$	$0.30^{+0.02}_{-0.02}$	$23.7^{+18.9}_{-6.2}$	57.7±3.2	420	14±0.8
A1736(H)	1^{+4}_{-1}	24^{+50}_{-24}	$7.9^{+15.3}_{-4.6}$	$0.02^{+0.03}_{-0}$	$0.01^{+0.01}_{-0}$	$47.8^{+63.9}_{-18.1}$	2.8±0.3†	21†	13±1.4†
A3558(H)	40^{+21}_{-31}	90^{+24}_{-52}	$2.4^{+2.9}_{-1.6}$	$0.8^{+0.4}_{-0.6}$	$0.08^{+0.04}_{-0.16}$	$41.4^{+14.4}_{-6.1}$	5.8±0.2†	56†	10±0.4†
A3558(P)	40^{+39}_{-10}	68^{+75}_{-20}	$10.2^{+0.3}_{-0.2}$	$1.0^{+0.9}_{-0.2}$	$0.1^{+0.09}_{-0.02}$	$35.9^{+1.1}_{-1.1}$	31.5±0.2	226	14±0.1
A3562(P)	37^{+26}_{-27}	95^{+55}_{-65}	$7.2^{+0.6}_{-0.5}$	$0.5^{+0.3}_{-0.3}$	$0.05^{+0.03}_{-0.03}$	$38.8^{+4.3}_{-3.0}$	17.3±0.3	105	16±0.3
A3571(H)	81^{+32}_{-34}	117^{+23}_{-27}	$4.1^{+0.7}_{-0.6}$	$1.8^{+0.6}_{-0.7}$	$0.1^{+0.03}_{-0.04}$	$26.4^{+3.0}_{-3.3}$	7.8±0.2†	81†	10±0.3†
A3571(P)	72^{+56}_{-31}	104^{+39}_{-24}	$5.8^{+0.9}_{-1.0}$	$1.6^{+1.2}_{-0.5}$	$0.09^{+0.07}_{-0.03}$	$27.0^{+3.1}_{-2.1}$	30.0±0.5	220	14±0.2
A1795(P)	381^{+41}_{-23}	177^{+19}_{-6}	$1.9^{+0.1}_{-0.1}$	$8.5^{+0.6}_{-0.2}$	$0.44^{+0.03}_{-0.01}$	$20.7^{+1.4}_{-1.5}$	31.9±0.3	133	23±0.2
A1795(H)	488^{+274}_{-166}	205^{+77}_{-54}	$0.8^{+0.2}_{-0.1}$	$10.4^{+0.4}_{-0.4}$	$0.54^{+0.0}_{-0.0}$	$16.4^{+8.0}_{-4.2}$	11.4±0.4	79	14±0.5
A2029(H)	554^{+215}_{-93}	179^{+47}_{-13}	$1.0^{+0.1}_{-0.1}$	$16.8^{+3.5}_{-1.1}$	$0.39^{+0.08}_{-0.03}$	$15.3^{+3.5}_{-2.6}$	13.4±0.3†	116†	12±0.3†
A2029(P)	556^{+44}_{-73}	186^{+19}_{-39}	$2.9^{+0.1}_{-0.1}$	$17.8^{+1.2}_{-2.9}$	$0.42^{+0.03}_{-0.07}$	$21.5^{+1.0}_{-1.1}$	44.5±0.5	251	18±0.2
A2052(P)	125^{+26}_{-6}	147^{+53}_{-3}	$2.5^{+0.1}_{-0.1}$	$1.9^{+0.4}_{-0.02}$	$0.51^{+0.11}_{-0.01}$	$26.0^{+1.9}_{-2.0}$	15.9±0.4	107	14±0.4
A2052(H)	102^{+108}_{-15}	134^{+71}_{-20}	$1.3^{+0.3}_{-0.2}$	$1.7^{+0.2}_{-0.1}$	$0.46^{+0.5}_{-0.3}$	$32.0^{+45.1}_{-7.7}$	5.1±0.3	49	10±0.6

04 to 1992 September 05 and with the *ROSAT* HRI from 1995 January 01 to 1995 January 11, with total exposure times of 5.36 and 15.5 ks respectively.)

At the same time that new cooling flows were discovered, three clusters considered to have small flows are now classified as non-cooling flows: A2319, A576 and A754. A2319 does not have the single peak typical of a cooling flow when observed with the HRI. The central cooling time is marginally consistent with the assumed

Table 5 – *continued*

Cluster	$\dot{M}$	$r_{\rm cool}$	$t_{\rm cool}$	$L(<r_{\rm cool})$	$\frac{L(<r_{\rm cool})}{L_{\rm bol}}$	t_{250}	$M_{\rm gas}$	$M_{\rm grav}$	$\frac{M_{\rm gas}}{M_{\rm grav}}$
(a)	(b)	(c)	(d)	(e)	(f)	(g)	(h)	(i)	(j)
MKW3(P)	175^{+14}_{-46}	171^{+9}_{-62}	$3.0^{+0.1}_{-0.1}$	$2.3^{+0.1}_{-0.6}$	$0.52^{+0.02}_{-0.14}$	$22.7^{+1.8}_{-1.6}$	$7.1\pm0.1^{\dagger}$	$58^{\dagger}$	$12\pm0.2^{\dagger}$
MKW3(H)	107^{+150}_{-50}	137^{+51}_{-7}	$1.1^{+0.9}_{-0.3}$	$1.4^{+0.4}_{-0.5}$	$0.32^{+0.09}_{-0.11}$	– – – –	– – – –	– – – –	– – – –
A2065(H)	13^{+14}_{-6}	56^{+22}_{-23}	$4.4^{+2.2}_{-1.3}$	$0.5^{+0.2}_{-0.2}$	$0.04^{+0.01}_{-0.01}$	$47.6^{+50.6}_{-16.0}$	$6.8\pm0.5^{\dagger}$	$90^{\dagger}$	$8\pm0.6^{\dagger}$
A2063(P)	37^{+7}_{-12}	95^{+13}_{-30}	$5.0^{+0.4}_{-0.3}$	$0.6^{+0.1}_{-0.3}$	$0.20^{+0.03}_{-0.1}$	$30.8^{+2.6}_{-2.9}$	15.8 ± 0.3	116	14 ± 0.3
A2142(P)	350^{+66}_{-133}	150^{+18}_{-49}	$5.2^{+0.4}_{-0.3}$	$13.0^{+1.8}_{-4.6}$	$0.24^{+0.03}_{-0.09}$	$17.2^{+0.8}_{-0.8}$	52.0 ± 0.8	369	14 ± 0.2
A2142(H)	286^{+57}_{-74}	152^{+23}_{-31}	$3.8^{+1.9}_{-0.8}$	$11.2^{+2.1}_{-2.8}$	$0.21^{+0.02}_{-0.02}$	$26.6^{+6.8}_{-4.2}$	47.2 ± 0.3	349	14 ± 0.1
A2199(H)	171^{+76}_{-28}	152^{+17}_{-23}	$1.2^{+0.2}_{-0.1}$	$3.0^{+0.2}_{-0.5}$	$0.47^{+0.03}_{-0.08}$	– – – –	– – – –	– – – –	– – – –
A2199(P)	154^{+18}_{-8}	143^{+17}_{-6}	$1.9^{+0.0}_{-0.1}$	$2.7^{+0.3}_{-0.1}$	$0.42^{+0.05}_{-0.02}$	$27.9^{+1.3}_{-1.5}$	20.8 ± 0.2	146	14 ± 0.1
A2204(P)	852^{+127}_{-82}	199^{+60}_{-44}	$3.1^{+0.1}_{-0.1}$	$40.1^{+4.6}_{-4.6}$	$0.75^{+0.09}_{-0.09}$	$19.4^{+1.2}_{-1.6}$	51.6 ± 1.2	339	15 ± 0.4
A2204(H)	843^{+245}_{-152}	181^{+88}_{-36}	$1.0^{+0.1}_{-0}$	$40.3^{+8.8}_{-4.2}$	$0.75^{+0.16}_{-0.08}$	$23.8^{+7.4}_{-4.5}$	$21.0\pm0.6^{\dagger}$	$186^{\dagger}$	$11\pm0.3^{\dagger}$
TRI AUST(P)	33^{+87}_{-33}	76^{+67}_{-76}	$10.8^{+7.1}_{-3.1}$	$0.7^{+1.7}_{-0}$	$0.03^{+0.06}_{-0}$	$24.4^{+1.9}_{-2.3}$	38.8 ± 0.7	197	20 ± 0.4
A2244(P)	244^{+49}_{-145}	148^{+20}_{-92}	$7.3^{+0.6}_{-0.5}$	$6.6^{+0.8}_{-4.0}$	$0.43^{+0.05}_{-0.26}$	$27.9^{+3.2}_{-2.5}$	35.7 ± 1.2	284	13 ± 0.4
A2256(P)	0^{+14}_{-0}	0^{+69}_{-0}	$15.0^{+4.0}_{-3.6}$	$0^{+0.2}_{-0}$	$0^{+0.01}_{-0}$	$35.5^{+3.9}_{-3.6}$	24.4 ± 0.4	154	16 ± 0.3
A2256(H)	0^{+16}_{-0}	16^{+69}_{-16}	$10.8^{+20.5}_{-9.1}$	$0.0^{+0.26}_{-0}$	$0^{+0.0}_{-0.0}$	$28.0^{+5.2}_{-3.9}$	26.5 ± 0.3	159	17 ± 0.3
OPHI(P)	127^{+48}_{-94}	129^{+22}_{-70}	$3.0^{+0.4}_{-0.3}$	$3.8^{+0.9}_{-2.6}$	$0.12^{+0.03}_{-0.08}$	$20.1^{+1.9}_{-1.8}$	37.6 ± 0.7	242	16 ± 0.3
OPHI(H)	34^{+10}_{-11}	72^{+7}_{-1}	$1.0^{+0.1}_{-0.1}$	$1.3^{+0.1}_{-0.01}$	0.04	– – – –	– – – –	– – – –	– – – –
A2255(P)	0^{+4}_{-0}	0^{+46}_{-0}	$36.9^{+21.0}_{-9.5}$	$0^{+0.1}_{-0}$	$0^{+0.01}_{-0}$	$51.2^{+7.0}_{-6.9}$	21.5 ± 0.5	171	13 ± 0.3
A2319(H)	4^{+103}_{-4}	34^{+100}_{-34}	$9.4^{+15.5}_{-3.7}$	$0.1^{+2.6}_{-0}$	$0^{+0.07}_{-0}$	$31.6^{+16.6}_{-8.6}$	$9.9\pm0.5^{\dagger}$	$103^{\dagger}$	$10\pm0.5^{\dagger}$
A2319(P)	20^{+61}_{-20}	53^{+59}_{-53}	$10.8^{+6.0}_{-2.9}$	$0.5^{+1.5}_{-0}$	$0.01^{+0.04}_{-0}$	$26.6^{+4.0}_{-3.0}$	37.0 ± 1.2	240	15 ± 0.5
CYG-A(H)	215^{+26}_{-22}	121^{+11}_{-12}	$1.7^{+0.1}_{-0.1}$	$8.1^{+0.3}_{-0.4}$	$0.49^{+0.02}_{-0.02}$	$28.5^{+9.4}_{-6.6}$	$9.0\pm0.3^{\dagger}$	$109^{\dagger}$	$8\pm0.3^{\dagger}$
CYG-A(P)	244^{+26}_{-22}	135^{+33}_{-34}	$2.6^{+0.1}_{-0.1}$	$9.3^{+0.8}_{-1.1}$	$0.56^{+0.05}_{-0.07}$	$28.5^{+3.6}_{-2.1}$	28.2 ± 0.8	201	14 ± 0.4
A3667(P)	0^{+11}_{-0}	0^{+63}_{-0}	$13.4^{+6.4}_{-3.4}$	$0^{+0.2}_{-0}$	$0^{+0.01}_{-0}$	$28.7^{+2.9}_{-2.3}$	24.8 ± 0.4	153	16 ± 0.3
A2597(H)	276^{+60}_{-3}	139^{+24}_{-26}	$1.4^{+0.1}_{-0.1}$	$8.2^{+0.7}_{-0.9}$	$0.61^{+0.05}_{-0.07}$	– – – –	– – – –	– – – –	– – – –
A2597(P)	271^{+41}_{-41}	152^{+67}_{-58}	$2.3^{+0.1}_{-0.1}$	$8.2^{+1.3}_{-1.9}$	$0.61^{+0.1}_{-0.14}$	$32.7^{+5.3}_{-2.9}$	22.9 ± 0.6	217	11 ± 0.3
KLEM44(P)	87^{+25}_{-19}	133^{+42}_{-27}	$2.3^{+0.6}_{-0.3}$	$1.1^{+0.3}_{-0.2}$	$0.49^{+0.13}_{-0.09}$	$83.8^{+121.0}_{-42.7}$	$4.3\pm0.2^{\dagger}$	$50^{\dagger}$	$9\pm0.4^{\dagger}$
A4059(H)	110^{+72}_{-33}	143^{+34}_{-12}	$1.9^{+1.14}_{-0.6}$	$1.5^{+0.4}_{-0.1}$	$0.32^{+0.09}_{-0.02}$	– – – –	– – – –	– – – –	– – – –
A4059(P)	130^{+27}_{-21}	153^{+19}_{-18}	$3.4^{+0.6}_{-0.4}$	$1.6^{+0.2}_{-0.2}$	$0.34^{+0.04}_{-0.04}$	$24.8^{+3.6}_{-3.6}$	19.6 ± 0.6	98	20 ± 0.6

age, and it possesses a radio halo (Hanisch 1982). A754 has a very disturbed X-ray morphology and a central cooling time in excess of 13 Gyr. It is known to be in a merging state (Henry & Briel 1995; Zabludoff & Zaritsky 1995; Henriksen & Markevitch 1996). A576 has a very flat surface brightness in X-rays when observed with the HRI. Although the cooling time is low, the mass deposition profile is perturbed and the value of the mass deposition rate is consistent with zero. From our analysis a clear cooling-flow/morphology relation appears in the B55 sample. This is consistent with the results of Buote & Tsai (1996), who found a quantitative correlation between the mass flow rate and morphology of 37 *ROSAT* PSPC clusters of the B55 sample. A similar analysis for the whole B55 sample will appear elsewhere (Peres, Buote & Fabian, in preparation).

All clusters which we classify as non-cooling-flows display signs of merger activity and/or a disturbed morphology in X-rays. Most notably, there are no examples, in the B55 sample, of a cooling flow cluster without a well-defined central galaxy at the bottom of the

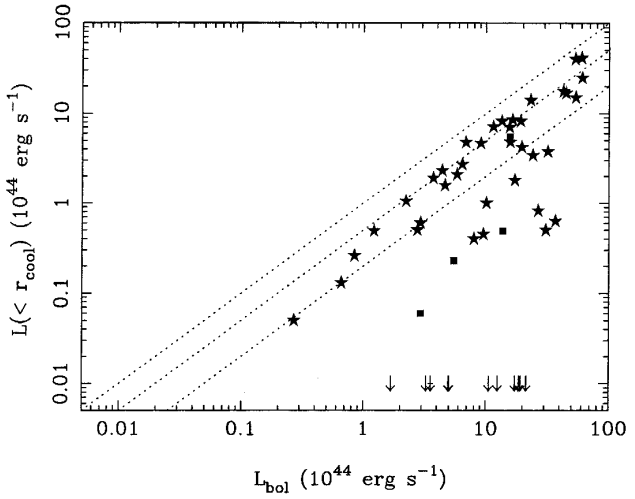

Figure 3. The luminosity from the cooling region, $L(< r_{\rm cool})$, is plotted against the X-ray bolometric luminosity from David et al. (1993). We note that, despite the dispersion, many clusters have $L(< r_{\rm cool})$ contributing to 50 per cent or more to the total X-ray luminosity. The dotted lines represent 20, 50 and 100 per cent of the cluster X-ray bolometric luminosity. Arrows represent non-cooling-flow clusters, which were assigned $L(< r_{\rm cool}) = 0.01$ for display purposes only.

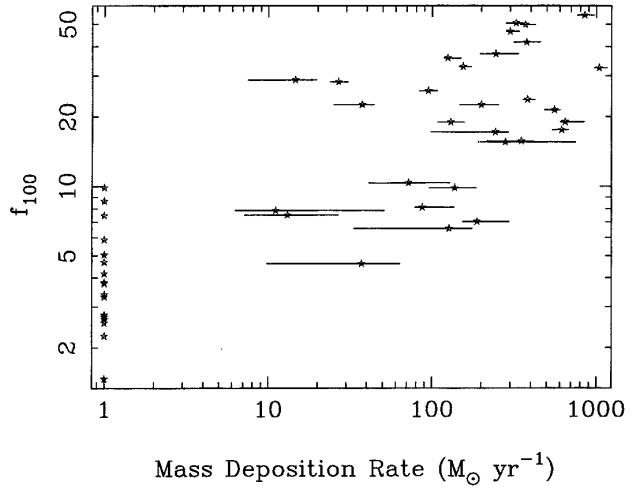

Figure 4. f_{100} is defined as the luminosity from a region of 100-kpc radius divided by the cluster X-ray bolometric luminosity given by David et al. (1993). We note that non-cooling flows (displayed here with $\dot{M} = 1\,{\rm M}_\odot\,{\rm yr}^{-1}$) have $f_{100} < 10$ per cent, whereas cooling-flow clusters have values of f_{100} ranging from 5 to 50 per cent. A trend of increasing f_{100} with mass deposition rate is indicated by the data.

cluster potential well.[7] The lack of *ROSAT* data for A2147 made us keep its classification as a non-cooling-flow cluster, since it had a large central cooling time and a mass deposition rate consistent with zero in the analyses of Edge et al. (1992) and White et al. (1997).

[7] The existence of non-cooling-flow clusters with a cD galaxy at the bottom of the potential well, e.g., A399 and A401, is very rare, leading to the interpretation of it as evidence of a previous phenomenon, which disrupted the flow (McGlynn & Fabian 1984; see Fabian, Peres & White 1997 for the specific case of A399/A401).

4.3 Fraction of cooling flows

The work of Edge et al. (1992) addressed this issue within the B55 sample, concluding that the fraction of cooling flow clusters is 70 per cent. However, they warned that it could be '*90 per cent, once the effect of different bin sizes is taken into account*'. In the study by Edge et al. (1992) only 36 clusters (65 per cent) had observations with a resolution better than 100 kpc. Correcton for that was made on the basis of a tendency for the cooling time to decrease with bin size as $t_{\rm c} \sim R^{1.5}$, which the authors inferred from their sample.

Here we confirm this tendency (cf. Fig. 6), but do not resort to it to establish the fraction of cooling flows in the B55 sample. With the improved spatial resolution of *ROSAT* we can resolve the central cooling regions of all clusters in the B55 sample, as can be seen from the short cooling times displayed in the histogram in Fig. 7.

We define here a cluster as a non-cooling-flow when the upper limit (90th percentile) to the central cooling time, as given by the deprojection procedure, is larger than the assumed age of the cluster (cf. Section 3 and Figs 6 and 5 above). By doing so, we conclude that the fraction of cooling flows in the B55 sample is 70 per cent (consistent with the 70–90 per cent estimates of Edge et al. 1992). Importantly, this is a conservative value, since we are not considering as cooling flows clusters for which the lower limit to the central cooling time is consistent with their assumed age (i.e., 13 Gyr). If we did include the clusters for which the central cooling time is consistent with 13 Gyr, then the fraction of flows would be ~90 per cent and we would have to include as cooling flows A119, A401, A399, A3158, A3266, A754, A3532, A1736, Triangulum Australis, A2256, A2319 and A3667. We prefer the first possibility here, because it does not include as cooling flow those clusters which are clear mergers, but whose central cooling time is just above the assumed age of the Universe; the ages of these clusters are certainly less than the latter.

In hierarchical scenarios for the formation of structures in the Universe clusters are assembled from smaller subunits through mergers. This complicates the estimation of the age of a cluster (and of its cooling flow age), which is one of the parameters used to determine the mass deposition rate. The fact that a cluster has suffered a merger does not necessarily imply that its cooling flow has an age equal to the lookback time of the merger, i.e., cooling flows may be older than their recently formed host cluster; as yet we do not know in detail how a merger affects an existing cooling flow.[8] In fact, if only approximately equal-mass, head-on collisions disrupt existing cooling flows, then the rarity of such events is reconciled with the high fraction of flows in our sample and can be used in future larger data sets to constrain cosmological scenarios.

A detailed investigation of the sensitivity of the mass deposition rate and fraction of cooling flows to individual cluster age would be ideal, but the complex history of formation of a cluster justifies the use of an average cluster age in our analysis. Assuming an average age of 13 Gyr for all clusters, we obtained a fraction of cooling flows of 70–90 per cent in the B55 sample. Since clusters are younger than 13 Gyr in all plausible formation scenarios, $\dot{M}$ and the fraction of cooling flows derived here are upper limits to their true value. Assuming an average cluster age of 6 Gyr yields a fraction of cooling flows equal to 65 per cent, whereas an age of 2 Gyr would still classify 45 per cent of our clusters as cooling flows. The values of $\dot{M}$ do not change by more than a factor of 3 when we assume an average cluster age of 5 Gyr. (With the exception of A644, A1650,

[8] A85 is the example of a cluster with clear substructure which harbours a strong cooling flow.

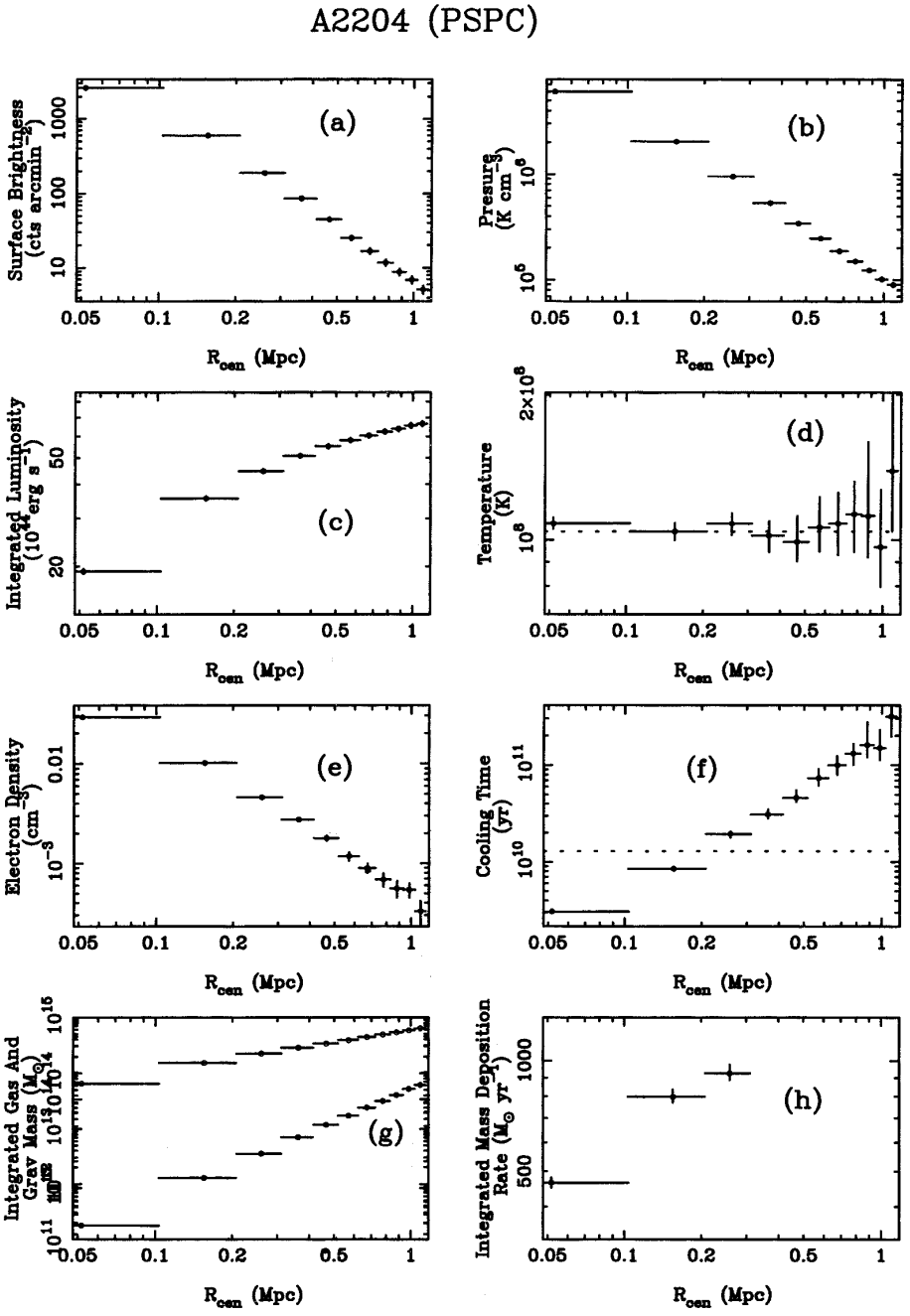

Figure 5. Summary of the deprojection results for the PSPC observation of the cluster A2204. Points in panels (a), (b), (c), (e) and (g) represent the mean value and 1σ errors (in each radial bin) from 100 Monte Carlo simulations. Points in (d), (f) and (h) represent the median and 10 and 90 percentile estimations from 100 Monte Carlo simulations. The dotted line in panel (d) marks the average temperature from David et al. (1993), and R_{cen} denotes the radius at the bin centre. Note that the potential is adjusted such as to produce a flat temperature profile.

A1651, A2142 and A4059, they either change by less than a factor of 2 or do not change appreciably.)

The high fraction of cooling flows found here is objectively defined and secure. The sample is not biased by the presence of large cooling flows, because it is flux-limited and constructed from observations with broad-beam instruments. All the clusters considered as cooling flows have very short central cooling times, and the fraction of flows in the sample remains basically unaltered if any other (reasonable) cosmology is selected (t_c/H_0^{-1} scales as $H_0^{0.5}$; cf. Fabian et al. 1984).

We have also computed the cooling time of the hot phase at a fixed radius (250 kpc) for as many clusters in our sample as possible. The value quoted in Table 5, t_{250}, is the cooling time of the bin encompassing the 250-kpc radius, and the quoted limits come from the Monte Carlo implementation of the deprojection analysis. The results are summarized in Fig. 8, from which is clear that all but two clusters have cooling times $13 < t_{cool}(250\,kpc) < 51$ Gyr. Fig. 8 was produced under the approximation that the limits to t_{250} were 1σ extrema of a Gaussian distribution (the limits were computed from the uncertainties provided by the deprojection analysis).

This exemplifies once more the need for high spatial resolution in

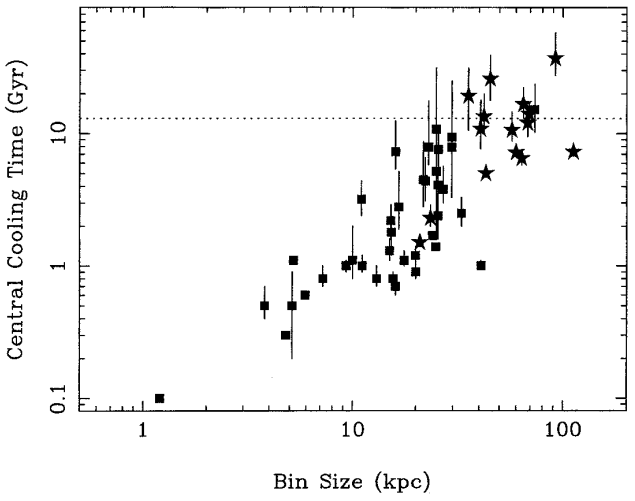

Figure 6. Central cooling time plotted against bin size for the B55 sample. The dotted line indicates the assumed age of the Universe (13 Gyr). From this plot it is evident that 70–90 per cent of the clusters in this sample are cooling flows. The trend of reduced central cooling time with increased resolution is also easily observed for the sample as a whole. The stars and squares represent PSPC and HRI observations respectively.

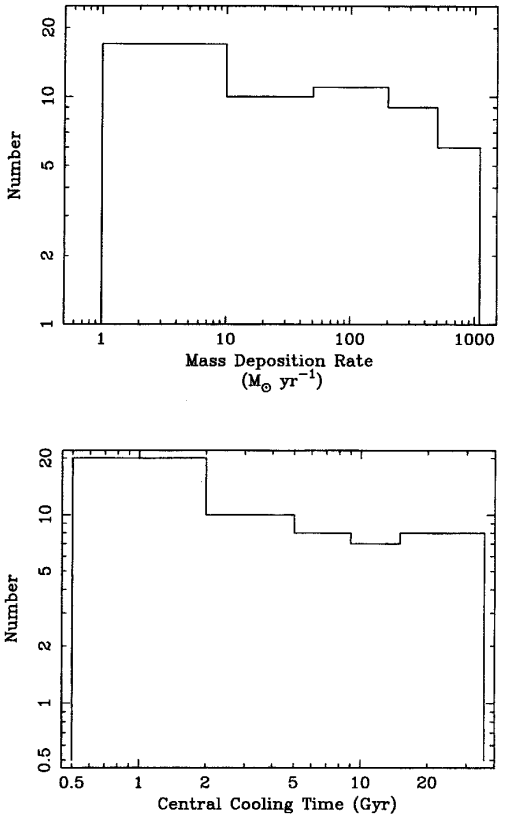

Figure 7. Histograms of mass deposition rates (top) and central cooling times (bottom) for the *ROSAT* observations of the B55 clusters. Note that changing the value of H_0 does not affect the fraction of cooling flows in the sample, because the ratio t_c/H_0^{-1} scales as $H_0^{0.5}$ (cf. Fabian et al. 1984).

the determination of a cooling flow, and provides a first estimate of the range of cooling times at around 250 kpc required from future numerical simulations of clusters of galaxies. The short cooling times at 250 kpc found in our sample are at odds with the values in

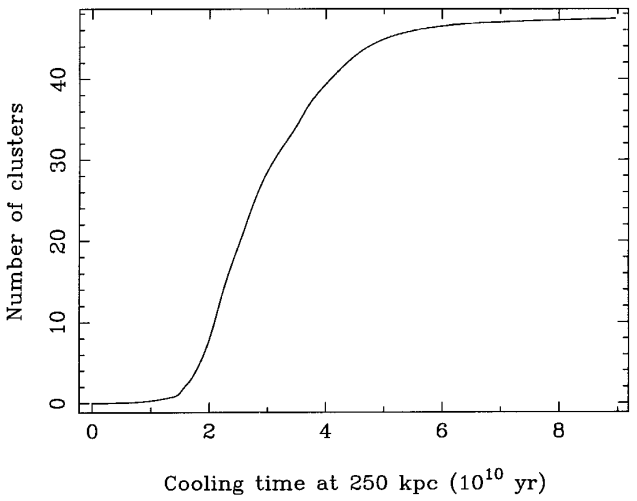

Figure 8. Cooling time at 250 kpc plotted against cumulative number of clusters. The plot shows 48 clusters for which the deprojection analysis was undertaken to a radius greater than 250 kpc. Each cluster was represented by a normalized Gaussian with dispersion given approximately by the deprojection limits. This plot shows that cooling times at 250 kpc from the centre of cooling-flow clusters are higher than the age of the Universe (13 Gyr) by not more than a factor of ~4.

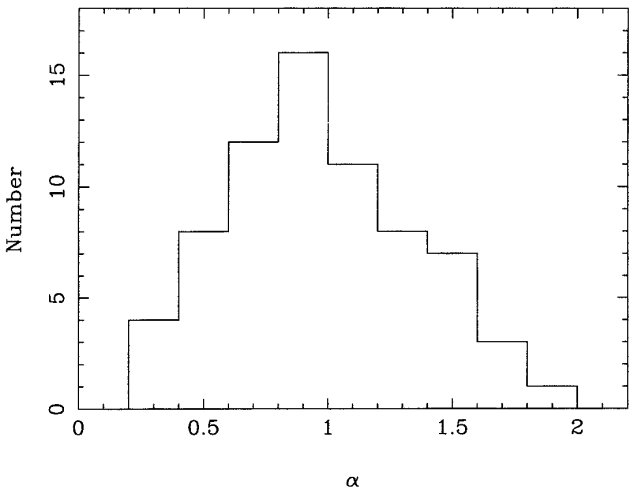

Figure 9. Histogram with the values of the slope of the integrated mass deposition profile for the B55 clusters. Note that the values scatter around the value $\alpha \sim 1$ predicted by multiphase models.

the simulations by Cen et al. (1995) and support the multiphase picture of the ICM where there can be gas cooling at and beyond 250 kpc. Future higher resolution data may demonstrate that some of the B55 clusters which have central cooling times larger than their assumed age (13 Gyr here) are non the less cooling flows, as indicated from the trend in Fig. 6 (although the trend is not guaranteed for every cluster individually, meaning that there are clusters for which we do not expect to detect a cooling flow even with data of improved resolution).

4.4 Mass deposition in cooling flows

Cooling flows are known to deposit large amounts of cool material throughout a cluster core (cf. Section 4.3 and Fig. 7). From Table 5 is clear that the accreted mass during the age of the flow,

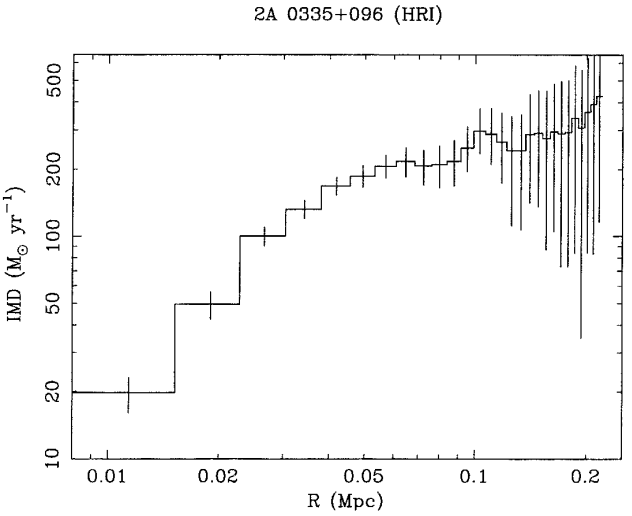

Figure 10. Integrated mass deposition (IMD) profile from the deprojection of an HRI observation of 2A 0335+096. Note that the slope changes clearly inside the cooling radius for the cluster ($r_{\rm cool} \sim 200$ kpc). Error bars are 10th and 90th percentiles from our deprojection analysis.

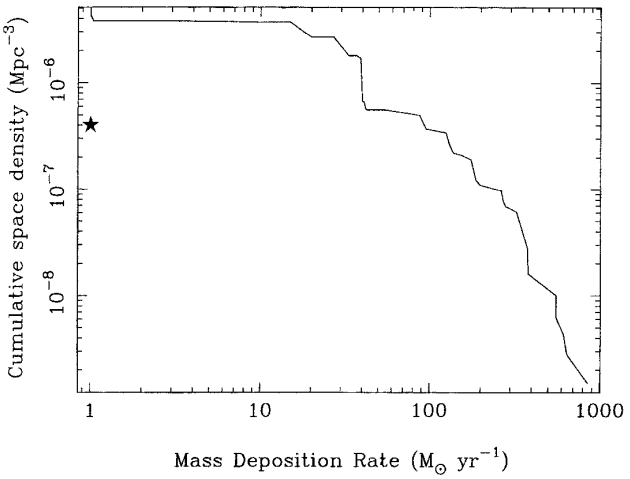

Figure 11. Cumulative space densitive of cooling flows from the B55 sample. The density is corrected for the selection function $|b| > 20°$. The space density of non-cooling flows, which were assigned here a mass deposition rate equal to one, is represented by a star.

$M_{\rm acc} \sim \dot{M} \times t_{\rm age}$, varies from 6×10^{10} to $6 \times 10^{12}\,{\rm M}_\odot$, if we assume an average cluster age of 6 Gyr and mass deposition rates of 10 and $1000\,{\rm M}_\odot\,{\rm yr}^{-1}$ respectively. We note from the discussion in the previous section that these estimates are not altered by more than a factor of ~6 when the cluster age is halved since $\dot{M}$ does not change by more than a factor of ~3. The mass accreted in large cooling flows ($> 200\,{\rm M}_\odot\,{\rm yr}^{-1}$) should not change by more than a factor of ~2. It would therefore be desirable to understand how this material is distributed over the cooling region, and how the cooling cores are distributed in the Universe.

We have studied the spatial variation of this material over the cooling regions of the B55 clusters with the HRI. To avoid contamination by small-scale substructure, we use the integrated mass deposition (IMD) profile which comes from the deprojection analysis and therefore has information on the azimuthally averaged mass deposition only. The shape of the IMD profile can be used to

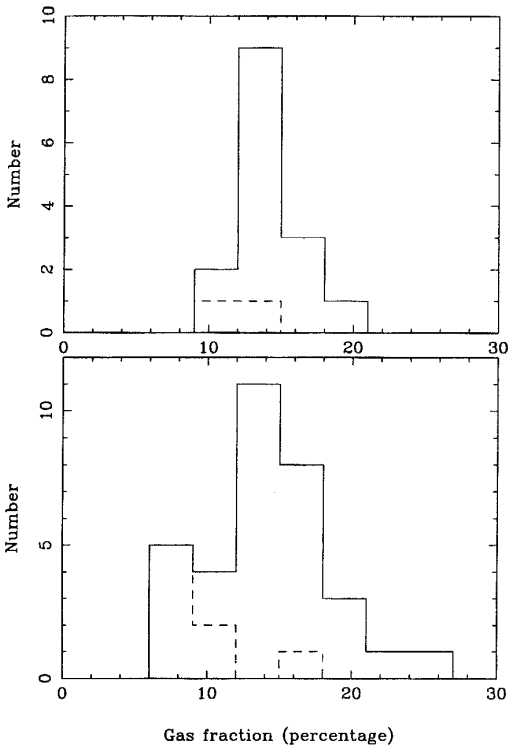

Figure 12. The histograms above show the baryon fractions for non-cooling-flow clusters (top) and for cooling-flow clusters (bottom). The dashed line in both panels represents the cases for which baryon fractions were calculated within 250 kpc only, whereas the solid line includes clusters with gas fractions computed within 500 kpc.

test the multiphase nature of the ICM and to trace the evolutionary history of the flow.

As for the first case, we know from previous work (Thomas et al. 1987; Nulsen 1986) that simple models of a multiphase flow would lead to an IMD profile of the form $\dot{M}(< r) \sim r^{\alpha}$, with $\alpha \sim 1$. We have used HRI and some PSPC observations to compute the slope of the IMD profile. For this purpose we have obtained the profiles from the deprojection algorithm with data points given by the mean and 1σ deviations. The profiles were then fitted with a power-law model. Only clusters with four or more bins inside the cooling radius were considered in the fitting procedure. Averaging the results for the whole set of observation analysed here yields $\langle\alpha\rangle = 0.95$, and a histogram of the values obtained can be seen in Fig. 9. The data are in good agreement with the simple multiphase models for the ICM. (Arnaud 1987 reached similar conclusions from a different sample.)

The possibility of using the IMD profiles as tracers of the evolutionary history of the flows was raised by Edge et al. (1992). They searched for the existence of 'breaks' of 'plateaus' in the IMD profiles, as indicative of previous phenomena which perturbed the flow. The detection of such features in the IMD profiles depends on how well we can sample the cooling region, for which HRI data is ideal. To search for a 'break' in the IMD profiles, we fit them with a broken power law in the same manner described above. We have noticed that many clusters show some kind of break in their IMD profiles, but only a few have breaks as apparent as in Fig. 10 (see also Irwin & Sarazin 1995); the clusters showing clear breaks in our analysis are 2A 0335+096, A426 and A496. In the case of 2A 0335+096, the cooling time at around 70 kpc, where the break occurs, is ~4–5 Gyr; in the suggestion by Edge et al. (1992) this is

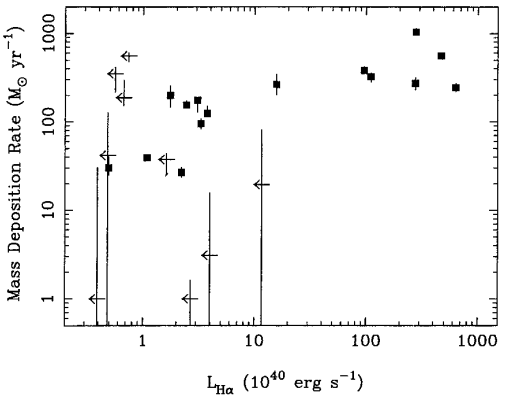

Figure 13. Correlation of Hα luminosities from the centres of clusters listed in Heckman et al. (1989) and the mass deposition rates inferred from our deprojection analysis. Note that for clarity we did not include the Virgo cluster in this sample. Points with left-pointing horizontal arrows represent upper limits for the observed Hα luminosity.

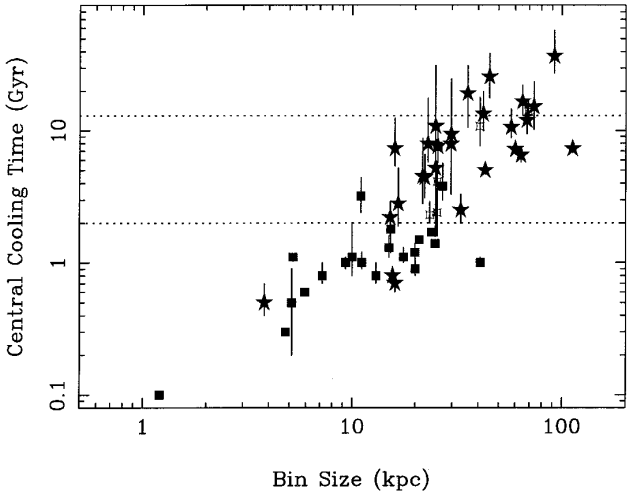

Figure 14. In the diagram above we denote clusters with emission lines by stars and clusters lacking emission lines by filled squares. Open squares are used to represent the clusters for which we have no information on the presence of emission lines. Emission-line clusters are situated predominantly below the line of central cooling time equal to 2 Gyr. Note there are only two emission-line clusters with central cooling times larger than 2 Gyr.

the approximate age of the flow (time since last disruption). Some of the breaks, however, occur in the outer bins of the IMD profiles, which can be attributed to fluctuations in the temperature profile, since $\dot{M}$ goes to first order as L_X/T. Allen & Fabian (1997) have proposed a method to estimate the age of cooling flows based on the spectral capabilities of the PSPC; this, however, needs high signal-to-noise data. Future high spatial resolution missions like *AXAF* will pin-down this issue.[9]

We have also used our recent data on the mass deposition by cooling flows to recalculate the space density of the flows (Edge et al. 1992). We have selected the clusters with galactic latitude larger than 20° and applied the usual procedure to compute the density function for a flux-limited sample. The result is presented in Fig. 11; the slope of a power law fitted between $\dot{M} = 10$ and $1000\,M_\odot\,yr^{-1}$ is ~ -1.8. Selection of clusters with $|b| > 10°$, instead of $|b| > 20°$, does not change the results significantly.

4.5 Gas fractions in cluster cores

Gas masses within 500 or 250 kpc for the B55 sample are presented in Table 5. They range from 2.5×10^{12} to $64 \times 10^{12}\,M_\odot$, constituting from 7 to 23 per cent of the total gravitational mass within this region.

Systematic errors due to our choice of potential and methodology are larger than the limits quoted from the deprojection analysis. However, since the baryon fraction in clusters (f_b) tend to increase with radius, we note that for our sample, $f_b > 6$ per cent. This conclusion is robust to the systematics mentioned above, agreeing with previously published results (White et al. 1993; White & Fabian 1995). It is important to stress that the gas fractions presented here do not include the contribution of baryonic material in cluster galaxies, representing lower limits to the baryon fractions in clusters.

We plot in Fig. 12 the gas fraction for cooling flows and non-cooling flows within 500 kpc from our analysis (250 kpc when information for 500 kpc is not available). This plot indicates that the non-cooling-flow clusters have a similar amount of gas, for a given mass, to cooling-flow clusters; the difference between them therefore resides in the spatial distribution of the gas in the core.

4.6 Comparison to optical and radio data

Cooling flows are the only simple route to explain the wealth of X-ray data on the centres of clusters of galaxies. From our previous analysis it becomes clear that (i) cooling flows are common and long-lived (fraction of at least 70 per cent in a flux-limited sample), and (ii) they deposit a large amount of cool material throughout a cluster core (about 40 per cent of the clusters in the B55 sample have $\dot{M} > 100\,M_\odot\,yr^{-1}$).

As a corollary of these points, we state that the cooling flow plays an important role in practically all phenomena happening in a cluster core. Historically, two phenomena have been traditionally linked to the cooling flow: optical emission-line nebulosity and radio activity from the BCG. A review of the role of cooling flows in these phenomena can be found in Fabian (1994).

Here we use the data from the work of Heckman et al. (1989) to investigate the role of the flow in the Hα luminosities of the BCG. We have changed the values of the published luminosities to match our assumed cosmological parameters. The results of a cross-correlation between the B55 and Heckman's sample (24 objects in common) is displayed in Fig. 13. We note that the weak trend suggested by Heckman et al. is maintained, i.e., Hα-luminous galaxies lie in the centre of large cooling flows, although this special cluster environment does not guarantee the existence of emission-line nebulosity in its BCG.[10] Finally, we note from Fig. 14 that clusters which display emission-line nebulosities have the shortest central cooling times in the sample: only two are greater than 2 Gyr.

Various generic scenarios have been put forward to understand the trend in Fig. 13. Crawford & Fabian (1992) suggest that the

[9] Numerical experiments are currently being undertaken with the aim of understanding how cluster collisions can affect the central cooling flow (e.g. Burns et al. 1994; Roettiger et al. 1997). Once the cause of disruption of a cooling flow is known, the incidence of cooling flows (Section 4.3) may be used to constrain cosmological scenarios.

[10] About 50 per cent of the cooling-flow clusters in the sample show line emission, whereas about 75 per cent of the clusters with emission lines display cooling flows with $\dot{M} > 100\,M_\odot\,yr^{-1}$. This trend can be used as an efficient method to search for large cooling flows at high z.

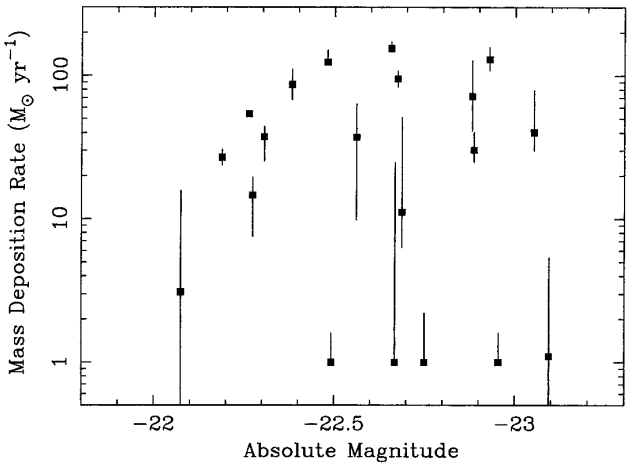

Figure 15. The lack of correlation displayed in the figure above indicates that the putative accretion population from the flow is not composed of stars with a normal IMF. This, however, does not eliminate the possibility of ongoing low-mass star formation. Despite the lack of correlation, there is the indication of a cut-off in the upper left part of the plot. Non-cooling flows were assigned $\dot{M} = 1$ for display reasons only.

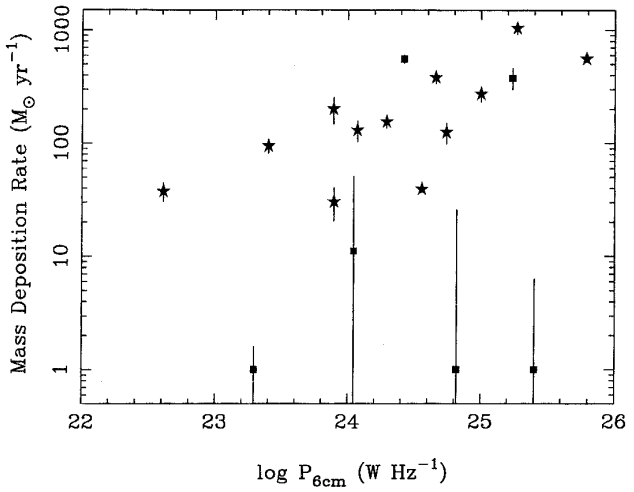

Figure 16. The plot above shows a correlation between the integrated power at 6 cm emitted by a cluster ($P_{6\,cm}$) and its cooling flow strength. Points to the right of the horizontal arrows represent upper limits for the observed radio power. Stars represent clusters with observed optical line emission; squares are used only to denote absence of emission lines or lack of information thereof. Non-cooling flows were assigned $\dot{M} = 1$. Data for which only upper limits exist were not used in the plot.

emission-line nebulosity is powered by mixing-layers in the multi-phase, turbulent ICM (Begelman & Fabian 1990). Since mixing layers occur where there is a population of cold clouds and where the hot ICM is most turbulent, we would expect emission-line nebulae to occur in the centres of large cooling flows. On the other hand, this scenario is consistent with the observation that some large cooling flows do not host emission-line nebulae (e.g., A2029), since the hot ICM may be in a quiescent state and/or most of the cold clouds may have formed stars already. It is interesting to remember that A2029 shows little excess absorption (White et al. 1991; Allen & Fabian 1997). Allen (1995) has presented new evidence for star formation at the centres of cooling flows, proposing that it can power the emission-line nebulae; early suggestions of this mechanism are found in Hu, Cowie & Wang (1985), Johnstone, Fabian & Bulsen (1987) and Heckman et al. (1989) among others. The role of magnetic reconnection in the emission-line nebulae has been re-investigated recently by Jafelice & Friaca (1996), and a recent detailed case study has been presented by Voit & Donahue (1997).

Optical images retrieved from the *Space Telescope* Digitized Sky Survey (DSS) were used to locate the optical counterparts to the peak in the X-ray emission from our cluster images. The optical position listed in Table 3 is the optical peak of the brightest galaxy nearest to the position of the X-ray peak. The listed offsets, $\Delta\theta$, are the modulus of the difference between the X-ray and optical positions, but no effort was made to correct the astrometry of the X-ray images. We note that most of the clusters with large offsets, $\Delta\theta > 25$ arcsec, do not have cooling flows: A119, A401, A3158, A754, A1367, A1736, A2256 and A3667. Most of the clusters, however, have optical positions consistent with the uncertainty in the position of their X-ray peaks: 65 per cent have $\Delta\theta \leq 10$ arcsec, and 85 per cent have $\Delta\theta \leq 25$ arcsec. The large values of $\Delta\theta$ for A1367 and A1736 stem from the flat X-ray surface brightness, without a clear centre. The extreme offset values of A2256 and A754 are due to the fact that the peak of the X-ray brightness does not correspond to the BCG in these merger systems, but to shocked regions of the ICM. The overall excellent agreement between the peak of the X-ray emission and the position of the BCG indicates that for most of the clusters in the B55 sample the X-ray gas is in a dymaically quiescent state, with the centre of the potential being occupied by a bright galaxy.

The appearance in the literature of a new, larger, photometrically homogeneous sample of BCGs (Lauer & Postman 1994) has prompted us to use our new cooling-flow results to search for a correlation between the strength of the flow and the optical light from the BCGs. This question has been investigated in the past in relation to the existence of a putative accretion population formed from the flow by Sarazin & O'Connell (1983), Schombert (1987), Thuan & Puschell (1989) and Edge (1991).

The sample by Lauer & Postman (1994) is volume-limited to $cz < 15\,000$ km s^{-1}, and it has 19 BCGs (out of 119) in common with our sample. We plot $\dot{M}$ against the absolute magnitude in Fig. 15, from which we notice that no evident correlation exists. The lack of correlation can be understood if star formation is skewed towards low-mass objects in the environment of cooling flows, but this is a much harder question to answer observationally (cf. Fabian 1994).

We have also cross-correlated the strength of the flow with the radio power from BCGs. We have used radio data on 17 BCGs by Ball, Burns & Loken (1993) and archival data obtained from NED, and the NVSS survey. From the archival information we could obtain the flux density of the central source, and then its luminosity at 6 and/or 20 cm. No simple correlation is evident from Fig. 16 (see also Fabian 1994) but, as we see, large cooling flows tend to have high radio luminosities (upper right corner of the diagram). This trend can be understood as a consequence of the high-pressure environment of cooling flows, which provide the working surface needed to produce the radio emission. When we split the data between clusters showing and clusters lacking emission lines, we note that the trend exists for the former only. Inspection of Table 3 shows that 19 out of the 22 clusters (i.e., 90 per cent) which display emission lines have radio emission from the centre, although only 19 out of 27 clusters (i.e., 70 per cent) displaying central radio emission have emission-line nebulosity.

Finally, we note a similarity between Figs 15 and 16. Both have a distinctive upper envelope with a roughly uniform distribution of data under it. In neither figure do we see large cooling flows with a

central cluster galaxy of small absolute magnitude or small radio power.

5 CONCLUSIONS

Our analysis of the X-ray properties of cluster cores with *ROSAT* showed that a cooling flow is the natural state of the cores of nearby clusters of galaxies. They constitue 70–90 per cent of the clusters in our flux-limited sample and deposit more than $100\,M_{\odot}\,yr^{-1}$ in about 40 per cent of the clusters. Large cooling flows can contribute more than 70 per cent of the cluster bolometric luminosity.

From our catalogue of ICM properties of the B55 sample we note that cooling times at the central bin are small, and that cooling times at 250 kpc from the cluster centre do not exceed ~4 times the age of the Universe (13 Gyr). We show that mass deposition in cooling flows have an approximately linear dependence on radius, and that clear breaks in some of the integrated mass deposition (IMD) profiles exist.

The cross-correlation of optical and radio properties with the strength of the flow yielded weak trends only. We noted that overall large cooling flows tend to have luminous BCGs and powerful radio sources at their centres, whereas no such rule exists for non-cooling flows.

ACKNOWLEDGMENTS

We are indebted to the members of the X-ray group and to S. Sigurdsson for valuable discussions. We thank in particular C. S. Reynolds and C. S. Crawford for providing us with some of the optical spectra for the analysis of the optical emission lines. CBP thanks Conselho Nacional de Desenvolvimento Cientifico e Tecnologico (CNPq – Brazil) for financial support, and acknowledges the receipt of an Overseas Research Studentship (ORS) award. ACF, ACE and SWA thank the Royal Society for support. RMJ and DAW thank PPARC for support.

This research has made use of data obtained through the High Energy Astrophysics Science Archive Research Centre Online Service, provided by the NASA-Goddard Space Flight Center, and the NASA/IPAC Extragalactic Database (NED) which is operated by the Jet Propulsion Laboratory, California Institute of Technology, under contract with the National Aeronautics and Space Administration. We also acknowledge the use of the on-line NVSS and FIRST catalogues. We thank an anonymous referee for useful comments on the manuscript.

REFERENCES

Allen S. W., 1995, MNRAS, 276, 947
Allen S. W., 1998, MNRAS, in press
Allen S. W., Fabian A. C., 1997, MNRAS, 286, 583
Allen S. W., Fabian A. C., Kneib J. P., 1996, MNRAS, 279, 615
Arnaud K. A., 1987, PhD thesis, Univ. Cambridge
Arnaud M., Rothenflug M., 1985, A&AS, 60, 425
Ball R., Burns J. O., Loken C., 1993, AJ, 105, 53
Begelman M. C., Fabian A. C., 1990, MNRAS, 244, 26P
Buote D. A., Tsai J., 1996, ApJ, 458, 27
Burns J. O., Roettiger K., Ledlow M., Klypin A., 1994, ApJ, 427, L87
Cen R., Kang H., Ostriker J. P., Ryu D., 1995, ApJ, 451, 436
Crawford C. S., Fabian A. C., 1992, MNRAS, 259, 265
David L. P., Slyz A., Jones C., Forman W., Vrtilek S. D., 1993, ApJ, 412, 479
Ebeling H., Vogues W., Bohringer H., Edge A. C., Huchra J. P., Briel U. G., 1996, MNRAS, 281, 799
Edge A. C., 1987, PhD thesis, Univ. Leicester
Edge A. C., 1991, MNRAS, 250, 103
Edge A. C., Stewart G. C., Fabian A. C., Arnaud K. A., 1990, MNRAS, 245, 559
Edge A. C., Stewart G. C., Fabian A. C., 1992, MNRAS, 258, 177
Fabian A. C., 1994, ARA&A, 32, 277
Fabian A. C., Willingale R., Pye J. P., Murray S. S., Fabbiano G., 1980, MNRAS, 193, 175
Fabian A. C., Hu E. M., Cowie L. L., Grindlay J., 1981, ApJ, 248, 47
Fabian A. C., Nulsen P. J., Canizares C. R., 1984, Nat, 310, 733
Fabian A. C., Crawford C. S., Edge A. C., Mushotzky R. F., 1994, MNRAS, 267, 779
Fabian A. C., Peres C. B., White D. A., 1997, MNRAS, 285, L35
Fadda D., Girardi M., Giuricin G., Mardirossian F., Mezzetti M., 1996, ApJ, 473, 670
Fukazawa Y., Ohashi T., Fabian A. C., Canizares C. R., Ikebe Y., Makishima K., Mushotzky R. F., Yamashita K., 1994, PASJ, 46, L55
Hanisch R. J., 1982, A&A, 111, 97
Heckman T. M., Baum S. A., van Breugel W. J. M., McCarthy P., 1989, ApJ, 338, 48
Henriksen M. J., Markevitch M. L., 1996, ApJ, 466, L79
Henry J. P., Briel U. G., 1995, ApJ, 443, 9
Hu E. M., Cowie L. L., Wang Z., 1985, ApJS, 59, 447
Irwin J. A., Sarazin C. L., 1995, ApJ, 455, 497
Jafelice L. C., Friaca A. C. S., 1996, MNRAS, 280, 438
Johnstone R. M., Fabian A. C., Nulsen P. E. J., 1987, MNRAS, 224, 75
Kaastra J. S., 1992, An X-Ray Spectral Code for Optically Thin Plasmas, Internal SRON-Leiden Report, updated version 2.0
Lauer T. R., Postman M., 1994, ApJ, 425, 418
McGlynn T. A., Fabian A. C., 1984, MNRAS, 208, 709
Mewe R., Gronenschild E. H. B. M., van den Oord G. H. J., 1985, A&AS, 62, 197
Mewe R., Lemen J. R., van den Oord G. H. J., 1986, A&AS, 65, 511
Nulsen P. E. J., 1986, MNRAS, 221, 377
Pesce J. E., Fabian A. C., Edge A. C., Johnstone R. M., 1990, MNRAS, 244, 58
Sarazin C. L., O'Connell R. W., 1983, ApJ, 268, 552
Schombert J. M., 1987, ApJS, 64, 643
Snowden S. L., McCammon D., Burrows D. N., Mendenhall J. A., 1994, ApJ, 424, 714
Stark A. A., Gummie C. F., Wilson R. W., Bally J., Linke R. A., Heiles C., Hurwitz M., 1992, ApJS, 79, 77
Tamura T. et al., 1996, PASJ, 48, 671
Thomas P. A., Fabian A. C., Nulsen P. E. J., 1987, MNRAS, 228, 973
Thuan T. X., Puschell J. J., 1989, ApJ, 346, 34
Voit M G., Donahue M., 1997, ApJ, 486, 242
Waxman E., Miralda-Escudé J., 1995, ApJ, 451, 451
White D. A., Fabian A. C., 1995, MNRAS, 273, 72
White D. A., Fabian A. C., Johnstone R. M., Mushotzky R. F., Arnaud K. A., 1991, MNRAS, 252, 72
White S. D. M., Navarro J. F., Evrard A. E., Frenk C. S., 1993, Nat, 366, 429
White D. A., Jones C., Forman W. R., 1997, MNRAS, 292, 419
Zabludoff A. I., Zaritsky D., 1995, ApJ, 447, 21
Zabludoff A. I., Huchra J. P., Geller M. J., 1990, ApJS, 74, 1